Draft version January 18, 2019
Typeset using LaTeX **twocolumn** style in AASTeX61

LOCAL SIMULATIONS OF MRI TURBULENCE WITH MESHLESS METHODS

Hongping Deng,[1] Lucio Mayer,[1] Henrik Latter,[2] Philip F. Hopkins,[3] and Xue-Ning Bai[4]

[1] *Center for Theoretical Astrophysics and Cosmology, Institute for Computational Science, University of Zurich, Winterthurerstrasse 190, 8057 Zurich, Switzerland*

[2] *Department of Applied Mathematics and Theoretical Physics, University of Cambridge, Centre for Mathematical Sciences, Wilberforce Road, Cambridge CB3 0WA, UK*

[3] *TAPIR, California Institute of Technology, Pasadena, CA 91125, USA*

[4] *Institute for Advanced Study and Tsinghua Center for Astrophysics, Tsinghua University, Beijing 100084, China*

(Revised January 18, 2019)

Submitted to ApJS

ABSTRACT

The magneto-rotational instability (MRI) is one of the most important processes in sufficiently ionized astrophysical disks. Grid-based simulations, especially those using the local shearing box approximation, provide a powerful tool to study the ensuing nonlinear turbulence. On the other hand, while meshless methods have been widely used in both cosmology, galactic dynamics, and planet formation they have not been fully deployed on the MRI problem. We present local unstratified and vertically stratified MRI simulations with two meshless MHD schemes: a recent implementation of SPH MHD (Price 2012), and a MFM MHD scheme with a constrained gradient divergence cleaning scheme, as implemented in the GIZMO code (Hopkins 2017). Concerning variants of the SPH hydro force formulation we consider both the "vanilla" SPH and the PSPH variant included in GIZMO. We find, as expected, that the numerical noise inherent in these schemes affects turbulence significantly. A high order kernel, free of the pairing instability, is necessary. Both schemes can adequately simulate MRI turbulence in unstratified shearing boxes with net vertical flux. The turbulence, however, dies out in zero-net-flux unstratified boxes, probably due to excessive and numerical dissipation. In zero-net-flux vertically stratified simulations, MFM can reproduce the MRI dynamo and its characteristic butterfly diagram for several tens of orbits before ultimately decaying. In contrast, extremely strong toroidal fields, as opposed to sustained turbulence, develop in equivalent simulations using SPH MHD. This unphysical state in SPH MHD is likely caused by a combination of excessive artificial viscosity, numerical resistivity, and the relatively large residual errors in the divergence of the magnetic field remaining even after cleaning procedures are applied.

Keywords: accretion, accretion disks — magnetohydrodynamics (MHD) — turbulence — methods: numerical

Corresponding author: Hongping Deng
hpdeng@physik.uzh.ch

1. INTRODUCTION

The turbulence instigated by the magneto-rotational instability (MRI) can transport angular momentum outwards thus enabling accretion in several classes of astrophysical disks such as those of dwarf novae, low mass X-ray binaries, and Active Galactic Nuclei (AGNs). Numerical MHD simulations are necessary to study this highly non-linear problem. Simulations of MRI range from local shearing box simulations, unstratified (e.g. Hawley et al. 1995, 1996; Sano et al. 2004; Simon & Hawley 2009) and stratified (e.g. Brandenburg et al. 1995; Stone et al. 1996; Miller & Stone 2000; Davis et al. 2010; Simon et al. 2011), to global simulations (e.g. Armitage 1998; Hawley 2000; Steinacker & Papaloizou 2002; Fromang & Nelson 2006; Parkin & Bicknell 2013; Zhu & Stone 2018). Three-dimensional simulations carried out with different grid-based codes, such as ZEUS (Hawley et al. 1995), Pencil (Brandenburg & Dobler 2002), RAMSES (Teyssier 2002; Fromang & Nelson 2006), ATHENA (Stone et al. 2008), and the spectral code Snoopy (Lesur & Longaretti 2007) report similar statistics for the turbulence.

Local MRI simulations are especially challenging because the saturated state appears to depend on the small-scale diffusion, be it physical or numerical. For instance, zero-net-flux simulations in unstratified boxes do not converge with increasing resolution, as turbulence reaches peak amplitude near the smallest resolvable scales. If physical sources of diffusivity are incorporated and resolved, turbulence can die out when the magnetic Prandtl number is too small (Fromang & Papaloizou 2007; Fromang et al. 2007). The latter dissipation is also sensitive to the vertical aspect ratio of the computational domain (L_z/L_x) (Shi et al. 2015). On the other hand, in net vertical flux simulations angular momentum transport depends on the magnetic Prandtl number once again, at least when the latter takes values of order unity (Meheut et al. 2015). Vertically stratified shearing box simulations without a net flux also suffer convergence problems (Bodo et al. 2014; Ryan et al. 2017). Adding a net vertical flux, however, can radically change the character of MRI turbulence as, for example, magnetic winds, can be launched. Some of the properties of these winds also suffer from non-convergence (Fromang et al. 2013; Bai & Stone 2013; Lesur et al. 2013). Finally, non-ideal MHD effects can suppress or radically alter the nature and strength of turbulence (see, e.g. Fleming et al. 2000; Turner et al. 2007; Bai & Stone 2011; Lesur et al. 2014; Bai 2014; Simon et al. 2015). Such effects are still under investigation.

Currently there are some published studies of the MRI as tests for mesh-free MHD methods (see,e.g., Gaburov & Nitadori 2011; Pakmor & Springel 2013; Hopkins & Raives 2015), but no systematic study of the MRI properties exists for the various standard flow and magnetic field configurations routinely examined with grid-based codes. This the case even though smoothed-particle magnetohydrodynamics (SPH MHD) (Springel 2010a; Price 2012) is already widely used in galaxy, star, and planet formation (Dobbs et al. 2016; Dolag & Stasyszyn 2009; Price & Bate 2007, 2008, 2009; Forgan et al. 2016). In codes without meshes or with arbitrary mesh geometries, minimizing the divergence of magnetic fields (Tricco & Price 2012; Hopkins 2016a) is a major challenge. Because proper minimisation of the divergence is hard to achieve, small "magnetic monopoles" can arise, leading to spurious magnetic field reconfiguration, reconnection, and artificial dissipation in neighboring domains.

On fixed, rectilinear, regular, non-moving grids, the *Constrained Transport* (CT) scheme (Evans & Hawley 1988) can maintain zero divergence to machine precision. Until recently, CT schemes had only been implemented for regular, non-moving meshes, but recently Mocz et al. (2014, 2016) successfully generalized the CT method to moving meshes that adopt a Voronoi tesselation as their volume partition (e.g. those in AREPO, Springel 2010b). Instead, most Lagrangian or quasi-Lagrangian methods, including moving-mesh as well as particle-based methods or mesh-free finite-volume methods, use the so-called "divergence cleaning" schemes to keep $\boldsymbol{\nabla} \cdot \boldsymbol{B}$ minimal (Powell et al. 1999; Dedner et al. 2002). Tricco & Price (2012) developed improved divergence-cleaning implementations in SPH (adapting the hyperbolic cleaning scheme from Dedner et al. 2002), and showed this could successfully reproduce some standard MHD tests, for example the Orszag-Tang vortex. But in non-linear MRI simulations, and in fact in any regime of MHD turbulence, effective divergence cleaning is especially difficult due to the complex, multi-scale field geometry, hence the latter methods are not guaranteed to work satisfactorily. SPH also suffers from known numerical dissipation sourced by various terms including the E0 error (Read et al. 2010), pairing instability (Rosswog 2015; Dehnen & Aly 2012) and incorrectly-triggered artificial viscosity (Deng et al. 2017a). It is well-known that this additional numerical dissipation impedes SPH's capability to model subsonic turbulence, even *without* magnetic fields (Bauer & Springel 2012; Hopkins 2015; Deng et al. 2017b).

The lagrangian mesh-less finite-volume (MFV) method was developed two decades ago (see, e.g., Vila 1999; Hietel et al. 2000) and further improved later on (see, e.g. Lanson & Vila 2008a,b). Recently it gained growing interest in the astrophysical community (see, e.g., Gaburov & Nitadori 2011; Hubber et al. 2017). Hopkins (2015) generalized the method in Gaburov & Nitadori (2011) to other mesh-free finite-volume Godunov schemes, including the closely-related "meshless finite-mass" (MFM) method. These methods, simlarly to moving mesh methods, attempt to combine advantages of grid-based and particle-based codes. In particular, they can describe subsonic hydrodynamical turbulence relatively well (with comparabale quality as grid-codes with regular meshes; Hopkins 2015), though at potentially greater computational cost, avoid advection problems in complex flow geometries that are better modeled in the lagrangian frame, respecting, for example, galilean invariance, and can be naturally extended to self-gravitating flows by exploiting accurate state-of-the-art gravity solvers, such as treecodes, which have native implementations for particle-based codes. Such mesh-less methods have been generalized to MHD (Hopkins 2016a), and in subsequent work by Hopkins (2016b) a constrained-gradient (CG) divergence cleaning scheme has been developed that can maintain a much smaller $\nabla \cdot \boldsymbol{B}$ (by $\sim$2 orders of magnitude) compared to hyperbolic divergence cleaning. These methods, as implemented in the public code GIZMO,[1] have in fact already been used to simulate the MRI in two-dimensional unstratified shearing sheets (Hopkins & Raives 2015), and these tests have demonstrated that it recovers the correct linear growth rates and behaves similarly to well-tested grid codes (e.g. ATHENA). However, how these methods perform in three dimensions, in stratified configurations, and/or during non-linear saturation, remain unclear.

In this paper, we carried out MRI simulations in both unstratified and vertically stratified shearing boxes, with both SPH and MFM MHD implementations as they are implemented in the multi-method GIZMO code, in order to explore the numerical requirements for these methods to treat the MRI in the non-linear regime. We focus on MFM as opposed to MFV or more general moving-mesh schemes (several of which are also implemented in GIZMO and can, in principle, use the same constrained-gradient divergence "cleaning" method) because MFM is designed, such as SPH, to conserve exactly the mass of fluid elements (i.e. there is identically zero advection), so the method is "purely" Lagrangian. This is perhaps the most challenging case for our purpose, since hybrid moving-mesh or MFV-type methods, in which the grid moves but mass fluxes are also allowed, effectively act as a smoothing of grid motion, thus interpolating between the "pure Lagrangian" (constant mesh-motion) and the "pure Eulierian" (fixed-grid) representation of a fluid. We also note that the effect of the initial noise in MFV, which appears to depend on how regular is the particle distribution in the initial conditions (Gaburov & Nitadori 2011), is poorly understood. In general, dependence of MRI properties on the numerical setup of the initial condition should be expected since MRI is extremely sensitive to numerical dissipation. Due to this added complexity of the initial condition design, although, in principle, MFV-type methods should be less prone to the effect of particle discretization noise during slope limiting as well as in the divergence cleaning step, we defer their scrutiny in the context of MRI to future work.

We will explore both the traditional "density-energy" formulation of SPH (named hereafter 'TSPH') (Springel 2005) and the more recently-developed "pressure-energy" formulation ('PSPH') (Saitoh & Makino 2013; Hopkins 2012). The SPH MHD used here represents the state-of-the-art implementation described by Price (2012) with the advanced artificial viscosity/resistivity switches developed in (Cullen & Dehnen 2010; Tricco & Price 2013) and divergence cleaning following (Tricco & Price 2012). In unstratified shearing box simulations, no significant density contrast is present and we expect TSPH and PSPH to perform similarly. Therefore, we did not run TSPH and PSPH comparisons for this particular setup. In the GIZMO MFM runs we adopt the constrained-gradient divergence cleaning of Hopkins (2016b).

We start, in Section 2, with a discussion of our shearing box implementation and the role of the smoothing kernel function. We also tested the resolution needed for accurate MRI eigenmode growth. In Section 3, we present unstratified shearing box simulations with and without net vertical flux and in short and tall boxes. Stratified shearing box simulations are described in Section 4 where we compare different simulation setups and the two methods, MFM and SPH. A discussion and conclusion follow in Section 5 and 6.

2. THE SHEARING BOX APPROXIMATION

The shearing box is a local expansion of the equations of motion widely used in MRI simulations to achieve high resolution (Goldreich & Lynden-Bell 1965; Hawley et al. 1995; Latter & Papaloizou 2017). One considers a small patch of a disk centered at a radius R and rotating at the angular velocity $\Omega(R)$. In the corotating frame one installs a Cartesian geometry at the box centre, us-

[1] The public version of the code, containing all the algorithms used here, is available at `http://www.tapir.caltech.edu/~phopkins/Site/GIZMO.html`

ing x and y to represent the radial and the azimuthal directions respectively. In compressible ideal MHD, the governing equations are

$$\frac{\partial\rho}{\partial t}+\boldsymbol{\nabla}\cdot(\rho\boldsymbol{v})=0, \tag{1}$$

$$\frac{\partial\boldsymbol{v}}{\partial t}+\boldsymbol{v}\cdot\boldsymbol{\nabla}\boldsymbol{v}=-\frac{1}{\rho}\boldsymbol{\nabla}(P+\frac{B^2}{8\pi})+\frac{(\boldsymbol{B}\cdot\boldsymbol{\nabla})\boldsymbol{B}}{4\pi\rho}$$
$$+2q\Omega^2x\hat{\boldsymbol{x}}-\Omega^2z\hat{\boldsymbol{z}}-2\boldsymbol{\Omega}\times\boldsymbol{v}, \tag{2}$$

$$\frac{\partial\boldsymbol{B}}{\partial t}=\boldsymbol{\nabla}\times(\boldsymbol{v}\times\boldsymbol{B}), \tag{3}$$

$$\frac{\partial\rho u}{\partial t}+\boldsymbol{\nabla}\cdot(\rho u\boldsymbol{v})=-P\boldsymbol{\nabla}\cdot\boldsymbol{v}, \tag{4}$$

where $\hat{\boldsymbol{x}}$ and $\hat{\boldsymbol{z}}$ are the unit vectors in the x and z directions, and ρ, u, P, c_s, $\boldsymbol{v}$ represent the density, specific internal energy, gas pressure, sound speed and velocity respectively. The tidal force term $2q\Omega^2x\hat{\boldsymbol{x}}$ in equation 2 comes from the expansion of the effective potential (gravitational plus centrifugal). The constant $q\equiv-d\ln\Omega/d\ln R$, and for a Keplerian disk $q=1.5$. The vertical component of the star's gravity is represented by $-\Omega^2z\hat{\boldsymbol{z}}$ which, if included, results in a vertical density stratification with a scale height of $H=c_s/\Omega$, where c_s is the initial sound speed. In simplified models examining motions confined near the disk midplane this term can be dropped. The ratio between the gas pressure and magnetic energy, $\beta\equiv P/(B^2/8\pi)$, is a dimensionless measure of the magnetic field strength which is widely used.

We assume an ideal gas equation of state (EOS),

$$P=\rho u(\gamma-1). \tag{5}$$

We choose $\gamma=5/3$ except noted where we set $\gamma=1.001$ to mimic an isothermal EOS. In particular, we have one stratified simulation with $\gamma=1.001$ to show how such a soft EOS exacerbates long-term numerical dissipation.

2.1. *Shearing Box Boundary Conditions*

The computation domain is a rectangular prism with sides of length L_x, L_y and L_z. In unstratified boxes, the domain is periodic in y and z, and shear periodic in x. These boundary conditions can be expressed mathematically for a fluid variable f as

$$f(x,y,z)=f(x+L_x,y-q\Omega L_xt,z), \tag{6}$$
$$f(x,y,z)=f(x,y+L_y,z), \tag{7}$$
$$f(x,y,z)=f(x,y,z+L_z). \tag{8}$$

They apply to all variables but the azimuthal component of the velocity, for which we need to add in the velocity offset due to the background shear,

$$v_y(x,y,z)=v_y(x+L_x,y-q\Omega L_xt,z)+q\Omega L_x. \tag{9}$$

The implementation of the shearing periodic boundary conditions in Lagrangian codes is relatively easy since we do not need to extrapolate fluid quantities to ghost zones as in grid-codes. When a fluid element ("particle") moves across the radial boundary it reappears at the other radial boundary with a velocity offset added to its azimuthal velocity.

In vertically stratified simulations we apply outflow boundary condition in the z direction by removing any element whose smoothing length is larger than 1.2H. This yields a density floor about 0.0002 in code units (see below).

2.2. *Equilibrium Tests and the Kernel Function*

The shearing box admits the following simple equilibrium: $\boldsymbol{v}=-q\Omega x\hat{\boldsymbol{y}}$, $\rho=$ constant. To test whether the code properly describes this state, in addition to the shearing periodic boundary conditions, we conduct an MFM simulation using this as an initial codition. We use a cubic box of one disk scale height per side. In the calculation we set $\Omega=1, c_s=1, \rho=1$. At a resolution of $48\times48\times48$ elements with the Wendland C4 kernel (200 neighbours, $N_{ngb}=200$), the equilibrium can be maintained to machine precision for the duration of the simulation ($\sim200\Omega^{-1}$) showing no signs of transition.

We next reran the simulation using the cubic spline kernel (55 neighbours) and found that the radial velocity becomes *non-zero* and the perfect lattice breaks into a glass configuration. The velocity errors are a few percent of the sound speed. In this case, elements form pairs as shown in figure 1. In SPH this pairing (or clumping) instability (Springel 2010a; Price 2012) happens with any kernel whose Fourier transform is negative for some wave vectors at sufficiently large neighbour number (Dehnen & Aly 2012). It would appear then that MFM also suffers a similar instability, if "too many elements" are included in the kernel radius of compact support (i.e. if one does not, as one should, use higher-order kernels with higher number of neighbors).[2] The Wendland C4 kernel does not suffer from these issues at this "enclosed neighbor number" (see e.g. Dehnen & Aly 2012). It also helps to keep elements well ordered, which is crucial for accurate gradient estimation in any unstructured method (Rosswog 2015). MRI turbulence

[2] The interpretation of the pairing instability in MFM is slightly different from in SPH – the kernel function is used in MFM to define the volume partition between neighboring resolution elements. If one takes a low-order kernel, say, the cubic spline, and forces its radius of compact support to enclose too many elements (such that the mean inter-element separation is much smaller than the kernel function width), the effective faces between elements essentially "overlap" into a single face (which becomes ill-defined).

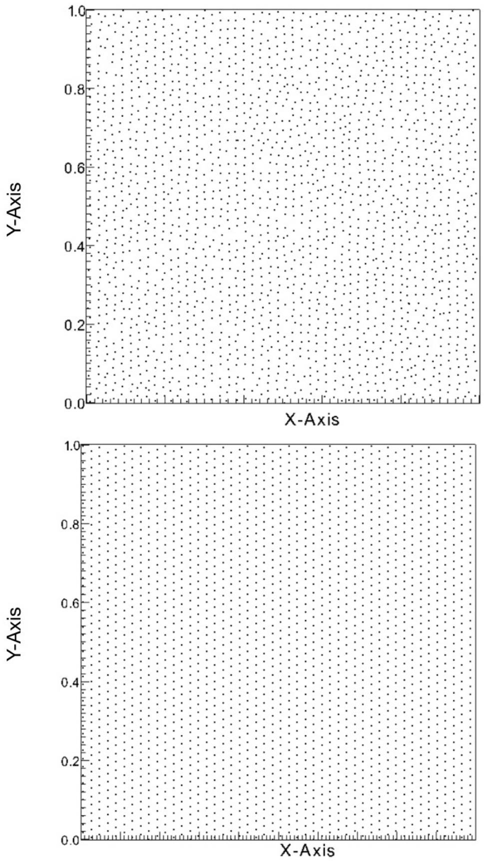

Figure 1. Resolution element ("particle" or "mesh-generating point") locations at $t = 8.4\Omega^{-1}$ in a *steady state* MFM run with the cubic spline kernel (top) and the Wendland C4 kernel (bottom). Elements form pairs in the simulation using the cubic spline kernel while the Wendland C4 kernel simulation maintains nice element order (initially cubic lattices are sheared)

is generally subsonic (except in the disk corona of stratified box), so we always use the Wendland C4 kernel to minimize numerical noise/dissipation (except when noted).

2.3. *Resolution*

In grid-code MRI simulations, the number of cells per fastest growing mode's wavelength is an important resolution metric (Hawley et al. 2011; Parkin & Bicknell 2013). We can define a quality parameter (Noble et al. 2010; Hawley et al. 2011) as

$$Q_z = \frac{\lambda_{MRI}}{\delta z} = \frac{2\pi V_{az}}{\Omega \delta z}, \qquad (10)$$

where V_{az} is the z component of the Alfven velocity and δz is the vertical grid size. λ_{MRI} is close to but not exactly the fastest growing linear mode's wavelength, $\lambda_{fastest} = \sqrt{16/15}\lambda_{MRI}$, in the presence of a net vertical flux. Perturbations with wavelengths smaller than $\lambda_{MRI}/\sqrt{3}$ are stable for the same configuration. We can easily extend the definition of Q_z to other coordinates. Q_z can be measured and averaged over the disk body during the saturated state. Regions where the plasma beta is high yield lower quality factors, and in these regions there may be insufficient resolution.

It should be noted that a quality factor, so defined, is a rather crude measure of how well the turbulence is resolved. First, it is based on the linear theory of the net-flux MRI set-up and hence may not be generally applicable; certainly its relevance for zero-net flux simulations is debatable. Second, it then only describes whether the input scale of the turbulence is resolved and has nothing to say about the ensuing turbulent cascade on smaller scales. If $Q_z \gtrsim 1$ then there is no inertial range to consider, and, in addition, the input and dissipative scales are directly adjacent: strictly, there is no real turbulence but rather a monoscale chaotic flow. Nonetheless, vertically stratified shearing box simulations indicate that $Q_z > 10, Q_y > 20$ ensures the convergence with resolution of certain large-scale average flow quantities (Hawley et al. 2011).

Unfortunately, we cannot apply the quality parameter to mesh-free codes directly, if nothing else because mesh-free codes are intrinsically adaptive and the denser regions are better resolved. To get an equivalent Q parameter we need to substitute the resolution scale h for δz in equation 10 (note h need not be the inter-element spacing). We now show how to compute h and hence Q.

In 3D simulations, the total number of elements enclosed in the radius of compact support of the kernel function, around the i'th element, is

$$N_{ngb} = \frac{4\pi}{3} H_1^3 n(\boldsymbol{x}_i) = \frac{4\pi}{3} H_1^3 (\rho_i/m_i), \qquad (11)$$

$$n(\boldsymbol{x}_i) = (\delta z)^{-3}. \qquad (12)$$

where H_1 stands for the kernel support radius. This is not, however, necessarily a good measure of h. A better definition for h in SPH is the standard deviation of the weighting kernel function $W(\boldsymbol{x}, H_1)$, as defined in Dehnen & Aly (2012),

$$\sigma^2 = \frac{1}{3} \int d\boldsymbol{x} x^2 W(\boldsymbol{x}, H_1). \qquad (13)$$

In MFM, for a well-chosen kernel where H_1 is chosen within a factor of a couple of the rms inter-particle separation so that faces are well-defined, the better definition of h is a face-area weighted inter-neighbor separation (where the face areas are themselves determined by the volume partition from the kernel function; Hopkins

2015). For the Wendland C4 kernel parameters adopted here, these give the fairly similar result $H_1/h = 2.2$, so we will use that value throughout. Finally we can define the meshless code quality factor:

$$Q_{cell} = Q_{sepr}(\frac{4\pi}{3N_{ngb}})^{\frac{1}{3}}\kappa, \tag{14}$$

where Q_{sepr} is the quality parameter calculated using δz and $\kappa \equiv H_1/h$ is related to the type of kernel used in the simulation.

The cubic spline kernel can achieve good density estimation with a small number of neighbours (say $N_{ngb} = 42$). It has a high rate of conversion between Q_{cell} and Q_{sepr}, $Q_{cell} = 0.9Q_{sepr}$. The Wendland C4 kernel ($N_{ngb} = 200$) has $Q_{cell} = 0.6Q_{sepr}$. As we stressed above, numerical dissipation is also related to the kernel used so we cannot generalize the grid-code resolution metric to mesh-free codes directly. Dedicated numerical experiments are needed.

2.4. *Channel flow growth*

The linear MRI eigenmodes in a net vertical flux are called channel flows. Being nonlinear solutions, these eigenmodes will grow to large and nonlinear amplitudes before being destroyed, in the first instance, by parasitic instabilities (Goodman & Xu 1994; Latter et al. 2009). A robust turbulence then ensues, which sometimes exhibits the recurrent generation and destruction of the channels. In this section we test the growth rate of the simulated channel flow to find the required resolution for linear MRI growth in both SPH and MFM. We compare these results with the finite volume Godunov code, ATHENA (Stone & Gardiner 2010), with second order reconstruction and either the Roe and HLLD solvers.

We initialize a box of size $H \times H \times H$, threaded by uniform vertical background fields of magnitude B_0. We set $\beta = 84$, so that the fastest growing channel mode just fits into the box, and $\gamma = 1.001$ so the gas is effectively isothermal. The initial amplitude of the channel mode is $0.001B_0$. The theoretical growth rate of the fastest channel mode is $0.75\Omega^{-1}$. The simulations are run for $8\Omega^{-1}$ so that the channel mode is smaller than $0.4B_0$ at the end of the simulation. We calculate the growth rate using the magnitude of the magnetic field at two consecutive snapshots taken every $0.5\Omega^{-1}$. The growth rate relative error is defined as

$$\max\{(s_i - 0.75)/0.75\} \tag{15}$$

where s_i is the ith measure of the growth rate.

In figure 2, we plot the growth rate error as a function of Q_{sepr} (number of elements per λ_{MRI}). As is clear, and to be expected, the errors decline with increasing

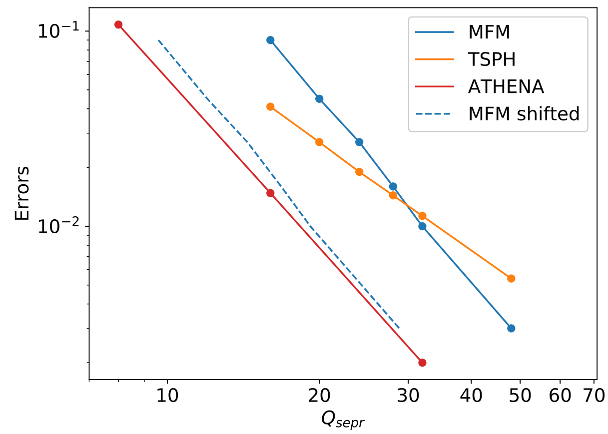

Figure 2. The growth rate errors in different MHD schemes. The errors decrease monotonically as the resolution increases. ATHENA (second order reconstruction) and MFM have the same scaling law while TSPH has a slower convergence. If we shift the MFM data leftwards by converting Q_{sepr} to Q_{cell} (see section 2.3) it almost overlaps with the ATHENA data.

resolution. They are less than 1% when $Q_{sepr} > 32$ in MFM. TSPH captures the MRI better than MFM in the low resolution simulations but it converges slower. It is known that SPH has zeroth order errors that only vanish when both Q_{sepr} and N_{ngb} approach infinity (N_{ngb} is fixed here) (Read et al. 2010; Zhu et al. 2015).

In order to avoid the pair instability, we initially chose the Wendland C4 kernel but this high order kernel smooths fluid variables over a relatively large range and results in a large effective cell size, and $Q_{cell} = 0.6Q_{sepr}$. For example, the $Q_{sepr} = 32$ simulations actually have only 19 effective cells per λ_{MRI}. At the same effective resolution ($Q_{cell} = 0.6Q_{sepr}$ for MFM), MFM and ATHENA work equally well. In principle, we can choose a more compact kernel in MFM since it doesn't have the zeroth order error in SPH (Hopkins 2015). For example, the cubic spline kernel has smaller N_{ngb} and a larger effective quality parameter Q_{cell} (see section 2.3), and indeed it outperforms the Wendland C4 kernel when the resolution is low. However, when $Q_{sepr} > 20$ the growth rate errors increase due to the pairing instability (which itself is resolution dependent, see Dehnen & Aly (2012)). This numerical noise (see section 2.2) can dominate over the weak channel mode in the early stage. The channel modes does eventually outcompete this noise but the errors in gradient estimation lead to extra dissipation (see section 4.2) which is hard to quantify.

3. UNSTRATIFIED SHEARING BOX SIMULATIONS

Table 1. Simulations, results and comments

Simulations	Initial fields	Boxsize	Resolution	MHD-methods	EOS	Sections/Figures	Ref
Unstratified	NZ	$H \times 6.28H \times H$	$64 \times 360 \times 64$	MFM	adiabatic	Sec 3.1/Fig 3	1
		$H \times 4H \times H$	48 elements per H	MFM/PSPH			
	ZNZ	$H \times \pi H \times H$	$64 \times 200 \times 64$	MFM	isothermal	Sec 3.2/Fig 4	2
		$H \times 4H \times 4H$	48/64 elements per H	MFM	adiabatic(c)	Sec 3.2.1/Fig 5	3
Stratified	B_y	$\sqrt{2}H \times 4\sqrt{2} \times 24H$	1.5M elements	TSPH/PSPH	adiabatic	Sec 4.2/Fig 7	4
				MFM	ad/iso	Sec 4.3/Fig 9	
			3M elements	MFM	adiabatic(c)	Sec 4.4/Fig 11	

Note— The following abbreviations have been used: **NZ** - Net vertical flux; **ZNZ** - Zero net vertical flux; **MFM** - meshless finite mass method with constrained gradient divergence cleaning; **TSPH** - Density-energy (traditional) formulation of SPH; **PSPH** - Pressure-energy formulation of SPH. Here we always uses the Wendland C4 kernel except one experiment run with the quartic spline kernel in figure 9. In stratified shearing box simulations, elements with smoothing length larger than 1.2H are clipped resulting in a density floor ~ 0.0002. Both SPH MHDs employee the Cullen & Dehnen artificial viscosity switch (Cullen & Dehnen 2010), the hyperbolic divergence cleaning of Tricco & Price (2012) and the artificial resistivity of Tricco & Price (2013). Furthermore **Adiabatic** runs use $\gamma = 5/3$, **isothermal** runs $\gamma = 1.001$, and **adiabatic(c)** runs apply an *ad hoc* cooling (see equation 20). We expect very fast turbulence decay due to numerical dissipation using isothermal EOS (see figure 9 & section 4.3). We always try to use an adiabatic EOS to minimise long-term numerical dissipation except when we want to enable direct comparison with previous studies.

Ref. 1. Hawley et al. (1996), 2. Fromang & Papaloizou (2007), 3. Shi et al. (2015), 4. Davis et al. (2010)

We summarize all the simulations we undertook in both unstratified and stratified boxes in table 1, which includes key parameters, physical and numerical configurations, comments, and references. Further details can be found in the referenced subsections.

3.1. *Net-Vertical-Flux Simulations*

We first ran an unstratified shearing box simulation with net vertical flux similar to the fiducial model of Hawley et al. (1995). This is the simplest 3D MRI setup. For such configuration we are able to reproduce the main features of previous grid-based simulations using high resolution MFM simulations. The box is of size $H \times 6.28H \times H$ and threaded by vertical fields with $\beta = 400$. We used a resolution of $64 \times 360 \times 64$ elements which corresponds to 28 elements per λ_{MRI}.

We added random velocity perturbations (5% of the sound speed) to the shear flow at initialisation. The simulation is run for 11 orbits with $\gamma = 5/3$. The box size also affects the simulated turbulence: smaller box tends to have stronger outbursts in the turbulent state (Bodo et al. 2008; Lesaffre et al. 2009). We set two other runs in a box of $H \times 4H \times H$ with $\beta = 330$ ($H = 2\lambda_{MRI}$), and with either PSPH and MFM using 48 elements per H.

To characterize the saturated turbulence we plot several density weighted-averaged quantities in figure 3. We note that we take the arithmetic average of fluid variables at all the MFM fluid elements so the average value is naturally density-weighted because of the adaptive nature of GIZMO. In unstratified turbulence, the density fluctuations are small so the density-weighted average should be close to the volume average in previous studies. This should be the case also for stratified turbulence, another situation in which we will apply this averaging method (see next section 4), because the stress is almost independent of the density when $|z| < 2\sqrt{2}H$ (Simon et al. 2011). In the $L_y = 6.28H$ simulation (red curves), both the magnetic energy and stresses are in good agreement with the results of Hawley et al. (1995), which were obtained with an Eulerian code. The ratio of the Maxwell stress to the magnetic pressure,

$$\alpha_M = \frac{\langle -2B_x B_y \rangle}{\langle B^2 \rangle}, \quad (16)$$

is about 0.5, namely similar to the aforementioned previous adiabatic calculations. The simulations in smaller boxes, $L_y = 4H$, show stronger bursts in stresses and magnetic energy because fewer active (non-axisymmetric) modes can fit in the box leading to artificial truncation of the nonlinear dynamic range, and, as a consequence, to the intermittent dominance of single channel modes.

The internal energy increases due to the turbulent dissipation. This is most significant in the two $L_y = 4H$ simulations as they exhibit the strongest bursts from channel flows. Indeed, since these flows achieve large amplitudes, when they break down a great deal of energy is dissipated into heat. The PSPH simulation, in particular, is some four times 'hotter' than the large box MFM simulation. The PSPH run undergoes also a much higher increase of internal energy compared to the equivalent MFM run (see Figure 3, upper right panel) due to stronger channel activity near the beginning of the run (signaled by the very large initial spike in the various diagnostics shown in Figure 3). The dominance of chan-

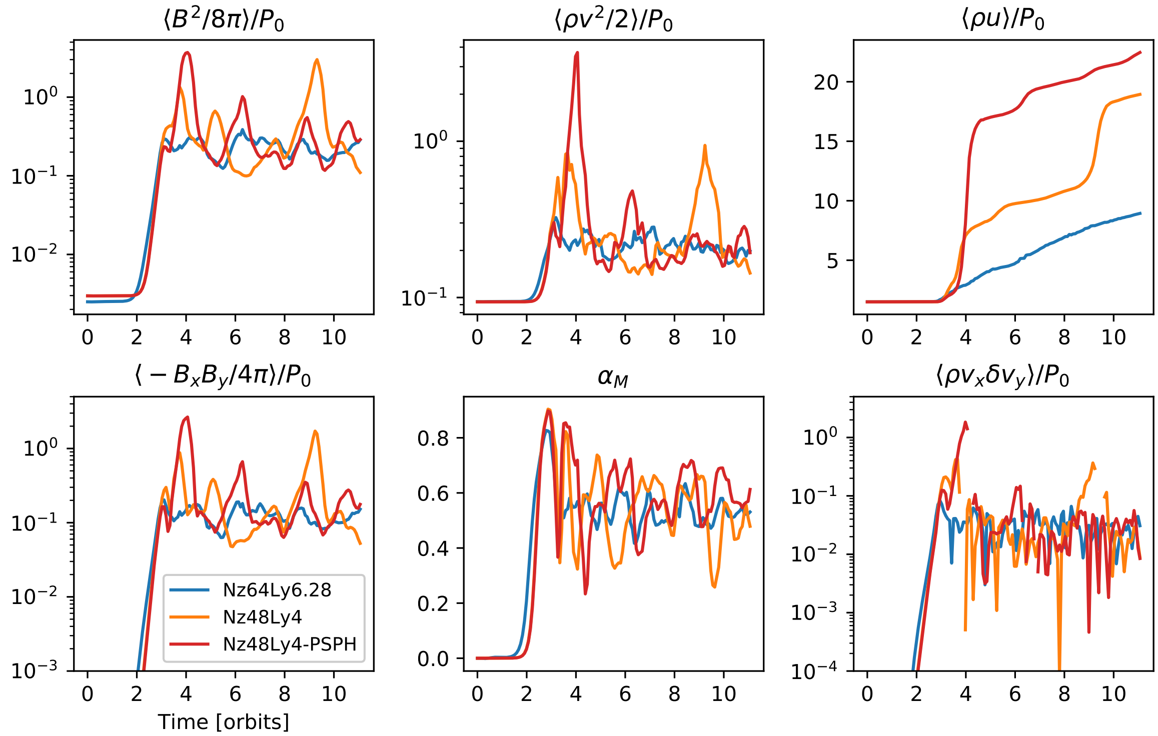

Figure 3. From upper left to bottom right corner, the time evolution of the averaged magnetic energy, kinetic energy, thermal energy, Maxwell stress, α_M and Reynold stress in the unstratified vertical flux simulations are shown (see text for the explanation of how average quantities are computed). Time is given in orbits. P_0 is the initial pressure. The MFM simulation with $L_y = 6.28H$ (red curves) gives results close to those of Hawley et al. (1996). The PSPH simulation with $L_y = 4H$ (black curves) has larger internal energy than the two MFM simulations. We note that the increasing internal energy leads to a larger plasma β and smaller outbursts.

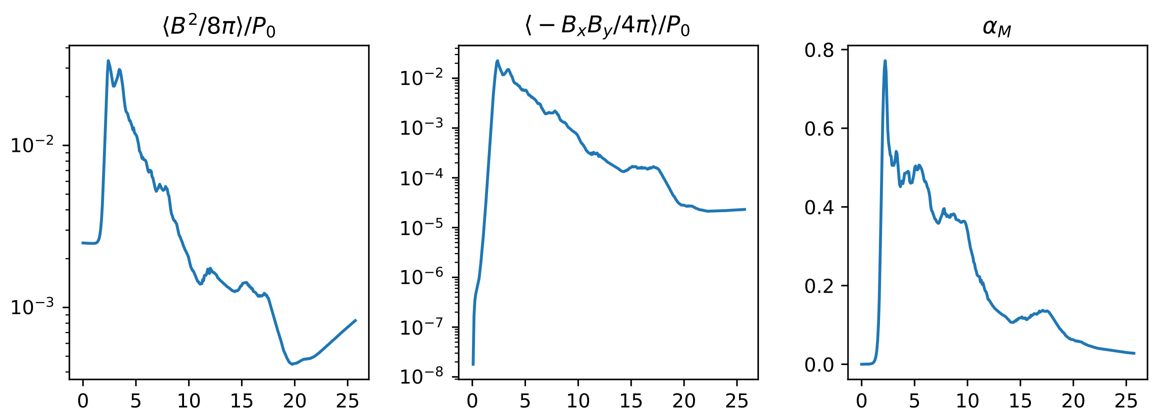

Figure 4. Time evolution of averaged magnetic energy, Maxwell stress and α_M in the zero net flux MFM simulation. Time is given in orbits. The magnetic field decays quickly and the Maxwell stress becomes nearly zero after about 20 orbits (see text) .

nels in the PSPH run early on suggests that the system is closer to marginal stability than in MFM; this is perhaps due to additional numerical diffusivity in PSPH. Note that the plasma β increases substantially as the gas is heated up, and the boxes will ultimately approach the incompressible zero-net-flux regime. This explains why, in general, the bursts become less powerful as the simulations continue. Finally, for the net-flux unstratified setup we only ran PSPH, and not TSPH, since there are no steep density gradients hence we expect no significant difference due to the actual formulation of the SPH hydro force.

At this point a cautionary remark is necessary on the issue of resolution matching between particle-based simulations, including MFM, and eulerian mesh-based simulations. While we have used, and motivated, the quality factor so far, another, simpler way to compare, which is often adopted in the literature, is to refer simply to number of resolution elements used in the simulation. However, while for the eulerian codes this would simply correspond to counting the number of cells, for particle-based codes this does not correspond to counting the number of particles. Indeed, in MFM as in SPH the resolution is determined by the kernel volume since this is where the interpolation occurs (which is instrumental to define a volume element in MFM). As we use a large number of neighbors, 200, in our MFM calculation, it turns out that, for example, in the net-vertical flux setups just discussed we have only 9 kernels along the vertical dimension, as opposed to 31 cells in the ZEUS simulations by Hawley et al. (1995). Therefore, if we use the straight metric of number of kernels per linear dimension, our MFM runs appear to have lower resolution than the grid-based runs. Furthermore, in Figure 2 this would correspond to shifting the dashed blue line to the left (by about a factor 2.2), so that the decrease of the error in the growth rate with resolution would appear to be faster in MFM relative to ATHENA. In the remainder we will keep using the quality factor but we should be reminded that the alternative,more straighforward way of comparing just discussed would, if anything, look more favourable towards MFM. Finally, we would like to point out that ZEUS, the code adopted by Hawley et al. (1995), has been shown to be quite diffusive, and is superseeded significantly by modern eulerian codes such as ATHENA in capturing the MRI, thereby the comparatively similar results of MFM should not be over-interpreted.

3.2. *Zero-Net-Vertical-Flux Simulations in a 'Standard' Box*

We run a standard zero-net-flux unstratified box simulation with MFM with no explicit physical dissipation terms (Stone et al. 1996; Fromang & Papaloizou 2007). We initialize a box of size $H \times \pi H \times H$ with $64 \times 200 \times 64$ elements, threaded by magnetic fields,

$$\boldsymbol{B} = B_0 \hat{\boldsymbol{z}} \sin(2\pi x/H). \tag{17}$$

The field strength B_0 is chosen that the volume averaged β equals to 400. We use an isothermal EOS ($\gamma = 1.001$) to align our choice with that of Fromang & Papaloizou (2007). MRI turbulence is sensitive to the nature of both physical and numerical dissipation. Without physical viscosity and resistivity, Fromang & Papaloizou (2007) found that zero-net-flux MRI turbulence was driven to smaller scales as resolution increased and there was no sign of convergence. Fromang et al. (2007) showed that the saturated state depended on the magnetic Prandtl number when a source of diffusivity, physical or numerical, is present; if this was too low, turbulence would decline after some period of time. With these problematic results in mind, we will now assess how well a zero-net-flux MRI setup can be modelled by a meshless code.

We plot the averaged magnetic energy, Maxwell stress, and α_M in figure 4. In contrast to MRI runs with grid codes, after an initial burst the magnetic fields and magnetic stress rapidly decay. There is no sustained turbulence, as in (Fromang & Papaloizou 2007) nor is there some period of MRI turbulence before decay, as in Fromang et al. (2007). It is true that MFM smooths fluid variables within a kernel, so the resolution (Q_{cell}) is actually lower than the standard simulation with $64 \times 200 \times 64$ grids in Fromang et al. (2007) (see section 2.3). A simulation with >128 elements per scale height is prohibitively expensive with MFM (see section 5.1). But even an 'ideal MHD' run undertaken with low resolution in a grid code can sustain MRI turbulence (Stone et al. 1996). Thus our result is disappointing.

One way to interpret it is to consider the relative sizes of the numerical resistivity and viscosity. At low resolutions, MFM should have a moderate numerical viscosity, ν (see appendix A) and relatively large numerical resistivity, η (see appendix B), as a consequence the effective numerical Prandtl number $P_m = \nu/\eta$ must be small (smaller than 1). It is then perhaps not surprising that the turbulence decays (Fromang et al. 2007). However, the fact that it decays so abruptly might point to a simpler reason: the numerical resistivity is just very large and prohibits turbulence of any kind past the initial spike. Indeed, our MFM run resembles in some respects the Fleming et al. (2000) run with a magnetic Reynolds number of 13000, which after an initial burst abruptly dies off.

3.2.1. *Zero-Net-Vertical-Flux Simulations in a Tall Box*

It has been shown that when the numerical domain is reshaped, so it exhibits a large vertical aspect ratio ($L_z/L_x \geq 2.5$), a new more vigorous and cyclical MRI dynamo emerges (Shi et al. 2015) (see also Lesur & Ogilvie (2008)). Importantly its saturated stress is independent of resolution. To test the effect of a taller

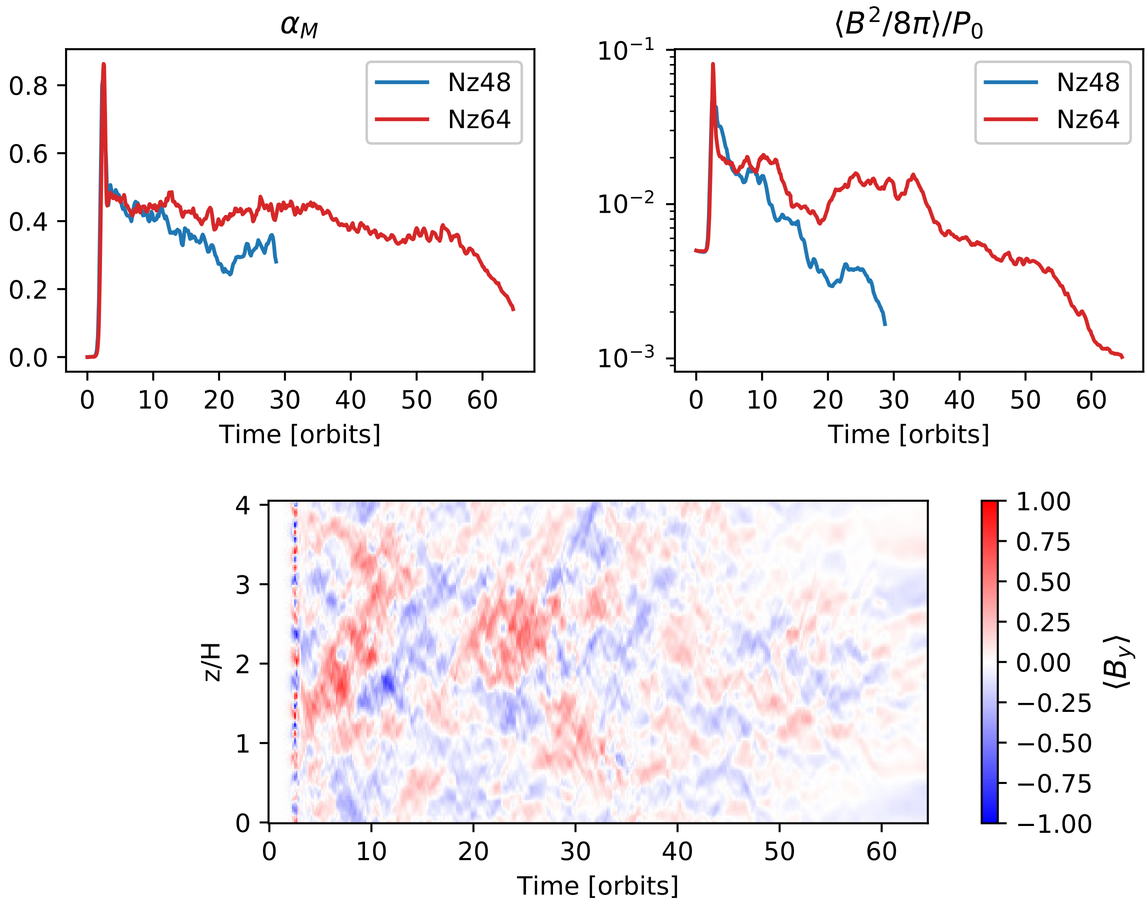

Figure 5. The time evolution of α_M and averaged magnetic energy in the zero net vertical flux tall box MFM simulation are shown in the upper panels. In the lower panel the temporal evolution of the averaged horizontal magnetic field of the Nz64 simulation is presented. The simulation (Nz64) with 64 elements per scale height shows a sign of convergence comparing to the fast decay of magnetic fields in the short box zero net flux simulation in figure 4. The pattern of the averaged azimuthal field is also similar to that of Shi et al. (2015). However, the magnetic fields eventually decays.

box, we redo the simulations in Section 3.2 in a box of size $H \times 4H \times 4H$. We present two simulations with 48 and 64 elements per scale height; their details are shown in figure 5. We set $\gamma = 5/3$ and add a cooling term in order to keep the internal energy roughly constant (see equation 20). The numerical dissipation is EOS-related and we expect very fast decay with the isothermal EOS (see section 4.3). This does mean, however, that we can't make direct quantitative comparison with Shi et al. (2015).

Initially our simulations exhibit turbulence as shown in Figure 5. Moreover they reproduce the averaged toroidal field patterns produced by Shi et al. (2015). However, while the turbulence is sustained for much longer than in the standard box, after some 30-40 orbits activity ultimately dies out. During the turbulent phase, the saturated $\alpha_M \sim 0.44$ in the higher resolution tall box simulation, but the averaged magnetic energy $\langle B^2/8\pi\rangle/P_0 \sim 0.01$ is much lower than the values (> 0.1) obtained with the ATHENA code (Shi et al. 2015). As a result, the stress ($\sim 0.006 P_0$) is also much smaller.

In tall box simulations, when the magnetic Prandtl number, $P_m \geq 4$ the saturated stress is independent of P_m while the turbulence vanishes for $P_m = 1$ with even 128 cells per scale height (Shi et al. 2015). While P_m effects might be at play in our simulations it should be noted that our 64 elements simulation is quite low resolution (elements are further smoothed within a kernel). Worse resolution leads to more rapid decay. It is likely that both meshless simulations possess too great a numerical resistivity to support a sustained MRI dynamo.

To summarize, the MFM simulations – at least with the current implementation of the method – do not allow to sustain MRI in unstratified zero-net flux simulations, either in short or tall boxes. This is probably the result of either too large a numerical resistivity, or, more generally, too low an effective P_m, at the resolutions we were able to access (see Section 5.1). It will be particularly interesting to explore both (a) higher-resolution MFM simulations (where the resistivity should be lower and P_m larger), and (b) simulations using other, closely-related schemes which are not completely "fixed mass" schemes but closer to moving mesh schemes (e.g. the MFV scheme or arbitrarily shearing-mesh schemes with the constrained-gradient divergence cleaning). We did not run zero-net-flux simulations with SPH, because there are many lines of evidence suggesting that it has an intrinsically larger numerical viscosity, and thus would yield higher Prandtl numbers, quite irrespective of the specific implementation of artificial viscosity (Bauer & Springel 2012; Deng et al. 2017a,b), and produces substantially larger magnetic field divergence with available divergence cleaning methods (see Section 4.1).

4. STRATIFIED SHEARING BOX SIMULATIONS

In this section we undertake simulations in the vertically stratified shearing box, in which the (leading order) vertical acceleration from the central star's gravity is incorporated. We initialise the simulations with a Gaussian density profile with uniform temperature

$$\rho(z) = \rho_0 \exp(-\frac{z^2}{2H^2}), \tag{18}$$

where $H = c_s/\Omega$ is a factor different from $\sqrt{2}c_s/\Omega$ in some previous work (Davis et al. 2010; Simon et al. 2011). Note that c_s is the initial sound speed; in adiabatic runs the sound speed (and hence scale height) will change. We adopt units so that $H = 1, \Omega = 1, c_s^2/\gamma = 1$ and use the adiabatic EOS with $\gamma = 5/3$. The density profile is sampled using the Monte Carlo method and then relaxed to a glassy configuration. The density errors in the disk body ($-3H < z < 3H$) are below the 1% level. We initialize azimuthal magnetic fields with $\beta = 25$ in a box of size $\sqrt{2}H \times 4\sqrt{2}H \times 24H$ (the box is extremely tall but no element has $|z| > 6$ in our simulations, see figure 12). Outflow boundary condition are applied but in fact there is no significant outflow and few elements are clipped. Random velocity perturbations $\sim 0.01c_s$ are added to seed the instability.

In our fiducial model we use 1.5M elements in total, leading to $h \sim 0.04$ at the disk midplane. However, due to the adaptive feature of our method, the resolution is lower the further away from the midplane. This helps in order to save some computational resource because high resolution is not needed in the MRI-stable disk corona with strong fields (see figure 12 and also Miller & Stone 2000). Yet, the nearly zero-flux MRI turbulence in the disk body still requires high resolution and is computationally demanding.

4.1. *Divergence Cleaning of Magnetic Fields*

Both SPH and MFM are not able to strictly maintain *exactly* solenoidal magnetic fields naturally, and thus must employ cleaning schemes to keep their divergences minimal. We try to quantify the efficacy of this procedure in this section before showing our main results.

We define the dimensionless divergence of magnetic fields as

$$divB = \frac{h|\boldsymbol{\nabla} \cdot \boldsymbol{B}|}{B}. \tag{19}$$

In our unstratified box simulations of section 3, the $divB$ diagnostic is smaller than 10^{-3} at the location of most fluid elements in MFM. Divergence control in the stratified shearing box MRI is more challenging, however. We run the fiducial model to compare the level of non-zero divergence in MFM with the CG cleaning (Hopkins & Raives 2015; Hopkins 2016a) and TSPH with the hyperbolic divergence cleaning (Tricco & Price 2012). In figure 6 the hyperbolic cleaning keeps $divB \sim 0.1$ in TSPH while the CG cleaning keeps $divB$ two orders of magnitude lower in MFM. Large $divB$ only occurs at the vertical boundaries and in the weak field regions in MFM; the vertical boundaries are poorly resolved because MFM fluid elements, which are built from particles, are fewer, but there the divergence should have negligible influence on the turbulent disk body since the correlation length of magnetic fields is smaller than H (Davis et al. 2010; Bai & Stone 2013). We also stress that the maps shown in Figure 6 are quite representative of the differences between SPH and MFM in our tests.

Summarizing, the CG cleaning method in MFM significantly outperforms its competitors here, and we shall see how this is important in the following subsection. As a word of caution, we note that, SPH methods that are recast at least partially in a finite-volume formulation, such as Godunov-SPH (Inutsuka 2002) , might be be amenable to implementations of the GC cleaning method. It would be interesting to explore the latter avenue in order to find out how much better an SPH method can perform once it is equipped with a superior divergence cleaning scheme.

4.2. *Unphysical Behaviour in SPH Simulations*

We present three SPH simulations, two of which are run with the Wendland C4 kernel and adiabatic EOS

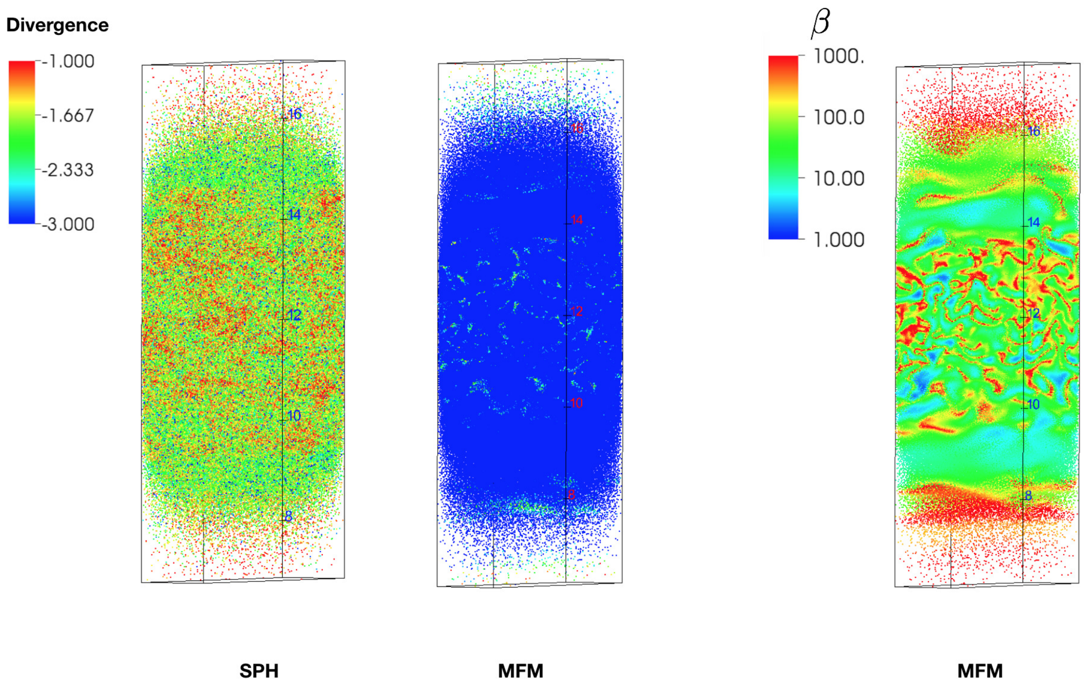

Figure 6. Typical $Log_{10}(divB)$ value in TSPH (PSPH shows similar results) and MFM. MFM with CG divergence cleaning maintains 2 orders of magnitudes smaller $divB$ than the hyperbolic divergence cleaning scheme used in TSPH. In MFM, most elements have $divB < 0.01$. Large $divB$ only occurs in the weak field ($\beta > 1000$) regions.

but using different SPH formulations. In figure 7 we plot α_M and the scaled magnetic energy versus time, in addition to space time diagrams of the horizontally averaged toroidal field. As is clear, the TSPH and PSPH simulations provide similar results. At first the MRI grows and expels the initial azimuthal fields to the disk corona where strong fields accumulate and are amplified (at about $\sim 60\Omega^{-1}$). Domains dominated by magnetic energy propagate from the corona to the disk midplane and ultimately the entire box is dominated by strong growing azimuthal fields ($\beta \sim 1$). Note that α_M is negligible from some 10-20 orbits, indicative that the MRI is quenched. At the end of the simulation the magnetic fields are at equipartition with the gas pressure, and almost entirely azimuthal with no turbulent activity. Simultaneously the disk expands vertically as it becomes magnetically supported. As is obvious, these simulations bear little resemblance to previous grid-code stratified shearing box simulations, which report robust subsonic turbulence in the disk body (Davis et al. 2010; Simon et al. 2011). To test if the strong fields persist in a more numerically dissipative setup, we reran the TSPH simulation with the quartic spline kernel (which has a noisier element distribution) and an isothermal EOS (see figure 9). We find that this TSPH variant in fact damps the turbulence faster and reaches the $\beta \sim 1$ state earlier.

We should note, the result that SPH grows strong toroidal fields is not unique to our simulation setup or code. Dobbs et al. (2016), using the SPHNG SPH code to simulate global galactic disk models, also reported unaccountable growth of magnetic fields. Likewise, similar behavior has also been seen in MHD-SPH simulations of disk formation in tidal disruption events with the code PHANTOM (Bonnerot, private communication). Both of these codes also implement the hyperbolic cleaning method from Tricco & Price (2012) in SPH. Stasyszyn & Elstner (2015) presents a detailed study that discusses the likely numerical issues: they consider 3D, global simulations of a differentially rotating disk with an initially pure-toroidal field, designed so the system is stable and should exhibit no field growth. Using more accurate (CT or vector-potential based) schemes they show that they recover this solution. But using SPH with similar hyperbolic divergence cleaning, they show that discretization error produces small radial field components, which couples to the rotational shear and amplifies this and in turn the toroidal field exponentially. They specifically show that the form of the SPH MHD induction equation leads (in essentially any internally-consistent SPH based cleaning scheme) to the divergence-cleaning *amplifying*

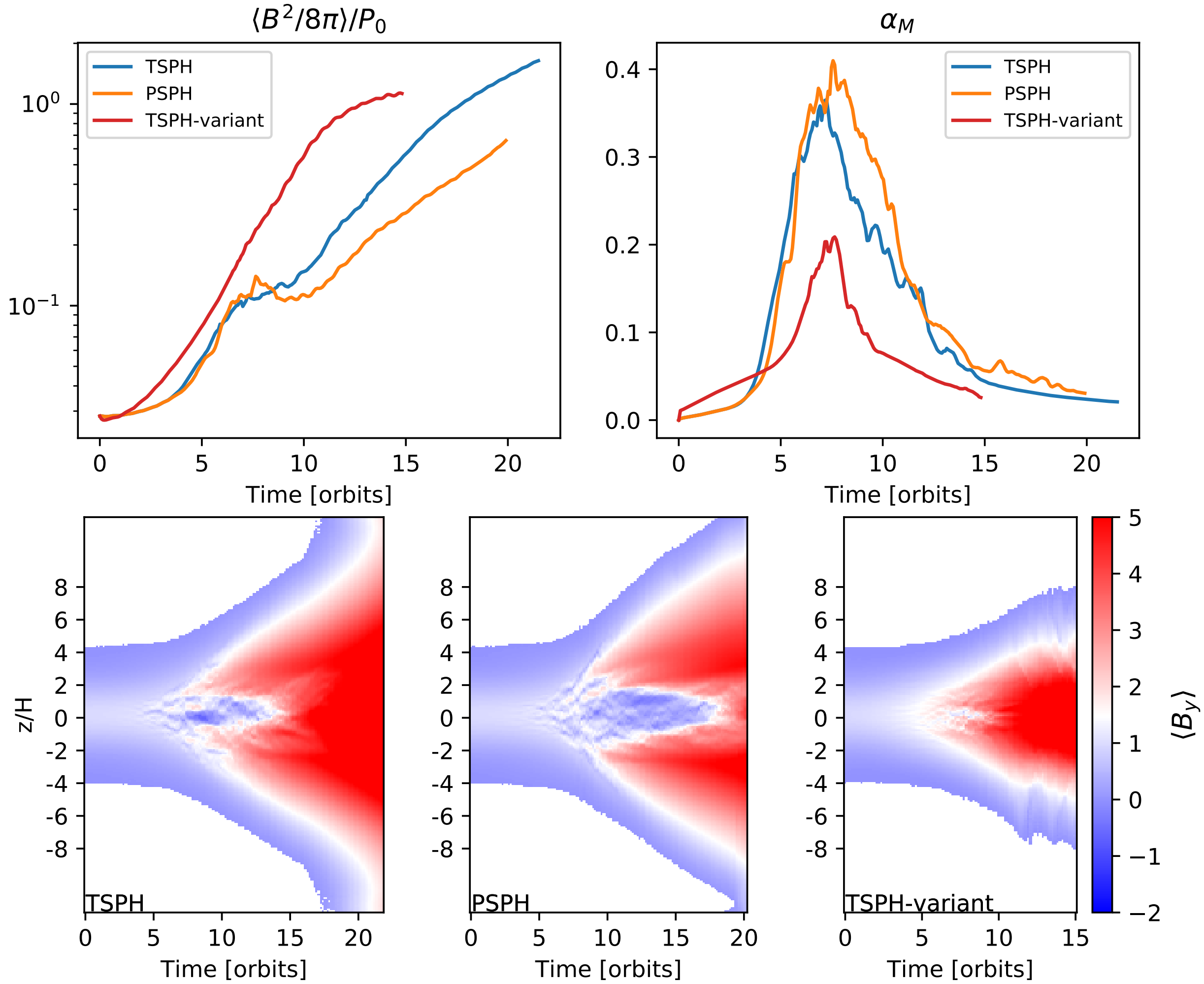

Figure 7. The evolution of the magnetic fields in the SPH MHD stratified shearing box simulations. The upper panels are the time evolution of the magnetic energy and α_M as noted. The lower panels show the time evolution of the horizontally averaged azimuthal magnetic fields. Strong toroidal fields grow through shear amplification of radial fields. Secondary instability cannot develop efficiently in the low resolution disk corona and the strong toroidal fields spread gradually to the disk midplane. The stratified box is eventually filled with strong toroidal fields ($\beta \sim 1$, stable to MRI) and the disk expands vertically. The PSPH and TSPH simulation are almost identical since their artificial viscosity damps subsonic turbulence similarly (Bauer & Springel 2012; Hopkins 2015). We add a more dissipative TSPH simulation, with the quartic spline kernel and isothermal EOS (see figure 9). The TSPH-variant simulation doesn't dissipate the strong toroidal fields but grows the fields even quicker due to larger numerical noise.

the vertical field, instead of *damping* the radial field, in order to locally restore $\nabla \cdot \mathbf{B} = 0$.

This demonstrates a few key ingredients that interact here: the particularly virulent form of this instability in SPH requires shear/differential rotation (either in global disk simulations or shearing boxes), non-zero radial, azimuthal, and vertical field components where there is a vertical gradient present that can offset the radial gradient (hence 3D, stratified simulations), and relatively-large $\nabla \cdot \mathbf{B}$ errors (note these are large here, with $divB \sim 0.01 - 0.1$).

We should also note that it is possible to construct divergence-cleaning schemes such as that in Tricco & Price (2012) which are total-energy conserving. In highly-idealized test problems, this will serve to limit the non-linear magnitude of any erroneous magnetic field amplification. However, in a shearing box or global thin disk simulation, there is an essentially infinite source of

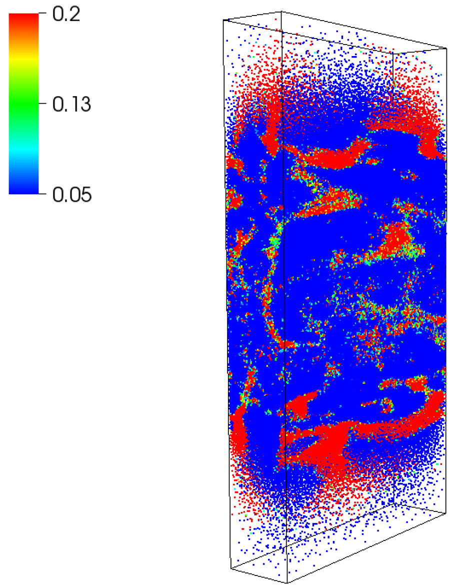

Figure 8. The artificial viscosity α_{sph} parameter in the PSPH run at $50\Omega^{-1}$ (see also figure 12). Relatively large artificial viscosity is triggered in the disk body where despite the fact that no shocks.

energy from shear, so this does not "rescue" the simulations from excessive numerical dissipation.

More generally, it is well-known that, without *any* divergence-cleaning, the $\nabla \cdot \mathbf{B}$ errors are violently numerically unstable: magnetic monopoles grow explosively and the amplitude of **B** is correspondingly rapidly-amplified. It is also well-established that this artificial, explosive field growth can occur even with divergence-cleaning, if the cleaning is not sufficiently accurate, or if it acts "too slowly" to respond to the growth rate. For example, Mocz et al. (2016) showed that using just Powell et al. (1999)-type (considerably less-sophisticated) divergence cleaning in even ordered meshes produces large artificial magnetic field growth (on essentially the Courant timescale) and much larger magnetic field strength, in idealized tests compared to CT methods.

Regarding the damping of turbulence, we should of course note that SPH requires artificial viscosity and resistivity to capture MHD shocks (Cullen & Dehnen 2010; Tricco & Price 2013, and references therein). It is well known that SPH tends to over-damp subsonic turbulence due to imperfectly triggered artificial viscosity (Bauer & Springel 2012; Hopkins 2015; Deng et al. 2017b). The GIZMO code applies an artificial viscosity switch similar to that described in Cullen & Dehnen (2010) with $\alpha_{min} = 0.05$ and $\alpha_{max} = 2$ (see Hopkins 2015, Appendix F2 for details) to suppress unwanted artificial viscosity. This switch works most efficiently in regions away from shocks and may not be effective at regions with large velocity derivatives (Deng et al. 2017a). In our SPH simulations, relatively large artificial viscosity with $\alpha_{sph} > 0.2$ is still triggered (see figure 8). Artificial viscosity certainly helps the turbulence dissipate. With damped velocity fluctuations, the MRI and its parasitic modes (Latter et al. 2009; Pessah & Goodman 2009) cannot grow efficiently. We therefore also explore what happens if we revert to the more dissipative artificial viscosity in GADGET2 (Springel 2005) and restart the TSPH simulation from $t = 50\Omega^{-1}$ (see figure 12); the turbulence does decay faster (as expected) and the strong toroidal fields develop more quickly. Thus, as expected, the MRI turbulence damping owes significantly to the artificial viscosity.

Artificial resistivity dissipates magnetic fields, and a switch to minimize artificial resistivity away from shocks was developed by Tricco & Price (2013). We here apply this artificial resistivity switch with $\alpha_{B,min} = 0.005$ and $\alpha_{B,max} = 0.1$. We choose this conservative $\alpha_{B,max}$ because the turbulence is subsonic (Hopkins & Raives 2015). We have re-run the TSPH simulation in figure 7 with $\alpha_{B,max} = 1$ (suggested by Tricco & Price 2013) and obtain similar results. The numerical resistivity in SPH MHD is evidently different from that of Riemann solvers (see appendix B).

4.3. *A Transient MRI dynamo in MFM Simulations*

Our MFM simulations use the same initial conditions as those of the SPH simulations. We present three simulations. The fiducial model is run with the Wendland C4 kernel and adiabatic EOS. In addition, to test the effect of the kernel function and EOS, we run two simulations with the quartic spline kernel ($N_{ngb} = 60$) and with an isothermal EOS. In the isothermal run we solve the energy equation instead of dropping it as done in Stone et al. (2008). To mimic the isothermal EOS we set $\gamma = 1.001$ so that the thermal energy dominates the total energy and large truncation errors affect the accuracy of magnetic energy calculation. This can cause the fast dissipation of the magnetic fields.

In figure 9 various quantities are plotted as functions of time. We see here that the MRI grows faster and reaches the magnetic pressure maximum quicker in the simulation with the quartic spline kernel (aqua) compared with the other two simulations. The quartic spline kernel is more compact and has a larger quality factor, Q_{cell} than the Wendland C4 kernel (see section 2.3). Although Dehnen & Aly (2012) shows that the quartic spline kernel is superior to the traditional cubic spline kernel it is still vulnerable to pair instability,

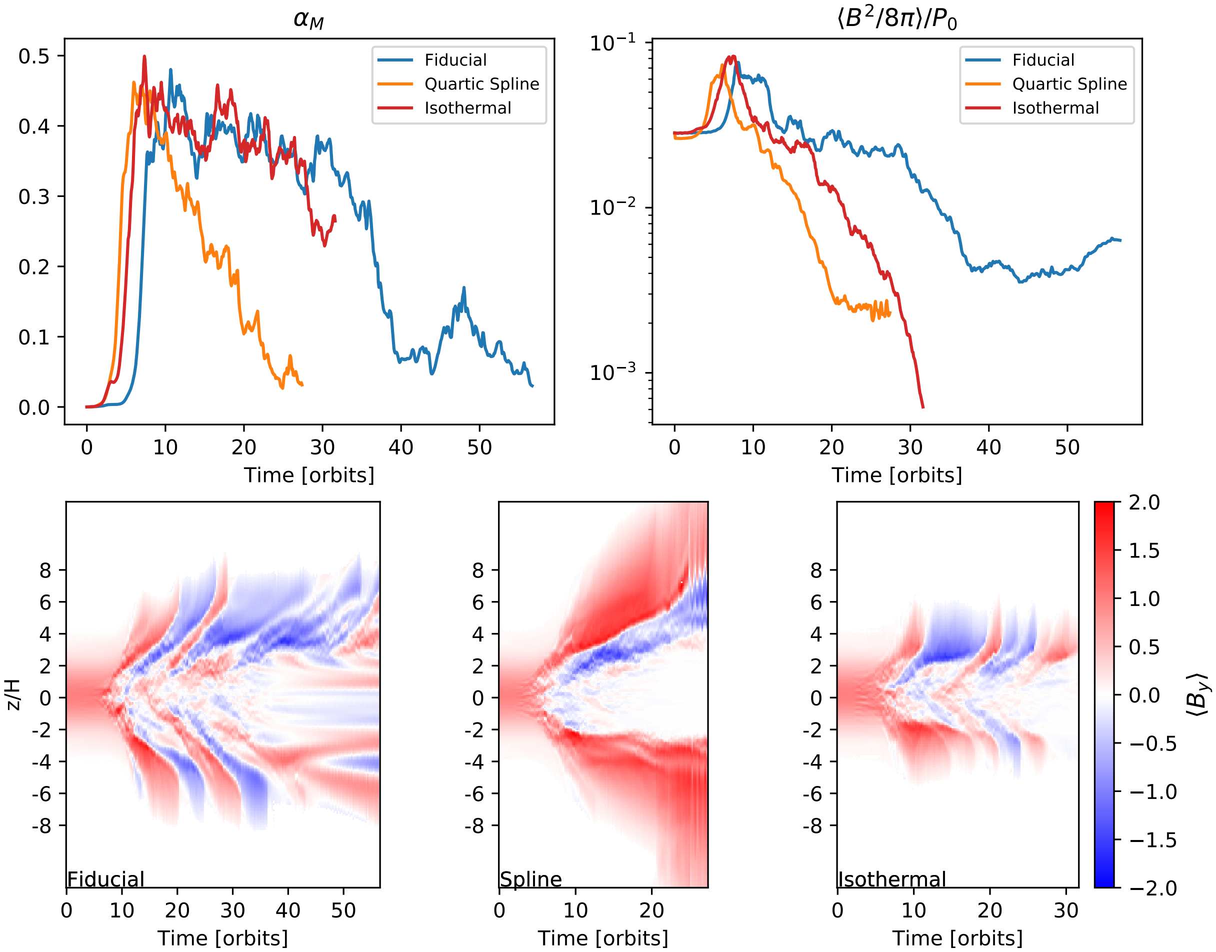

Figure 9. The evolution of the magnetic fields in the MFM stratified shearing box simulation with 1.5M elements and different setups. The upper panels are the time evolution of α_M and the magnetic energy as noted. The lower panels show the time evolution of the horizontally averaged azimuthal magnetic fields. In the fiducial run, both the saturated α_M and averaged azimuthal field pattern (butterfly diagram) agrees well with previous grid-code simulations (Hawley et al. 2011; Simon et al. 2011) in the early 30 orbits. The fields decay later partially due to the expansion of the shearing box and thus decrease of the resolution (see figure 10). The simulation with the quartic spline kernel cannot reproduce the butterfly diagram due to numerical noise at the kernel scale, and the magnetic fields decay rapidly. The isothermal stratified shearing box with $\gamma = 1.001$ doesn't expand vertically and thus maintains the resolution. However, the truncation error in the energy equation eventually leads to magnetic field dissipation.

which introduces numerical noise in gradient estimation. It would appear that this noise provides a significant degree of numerical dissipation because we find that the MRI dies quickly after its initial spike. The isothermal and fiducial adiabatic runs are qualitatively similar: both can sustain MRI turbulence for a period of some 30-40 orbits before dying.

In the first 30 orbits the fiducial model successfully reproduces the quasi-periodic ($\sim$10 orbits) butterfly pattern of the averaged azimuthal fields. Note, however, that the butterfly diagram becomes erratic at $\sim 200\Omega^{-1}$ as seen in other thermal MRI runs (Gressel 2013; Riols & Latter 2018). The saturated $\alpha_M \sim 0.4$ and $\langle B^2/8\pi \rangle/P_0 \sim 0.01$, however, are both in agreement with previous isothermal grid-codes' results (Simon et al. 2011). During the simulation, the box expands vertically due to accretion heating leading to a decrease of resolution in the disk body. In figure 10, the density at the disk midplane drops to 0.6 at $200\Omega^{-1}$ which corresponds to 1.2 times larger mean fluid element

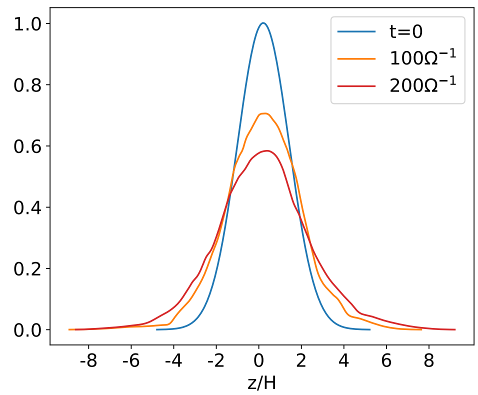

Figure 10. The vertical density profile of the fiducial stratified shearing box MFM simulation at different time. The box expands vertically and at $200\Omega^{-1}$ the midplane density drops to 0.6 (the mean element separation becomes 1.2 times larger).

separation. The decrease in resolution certainly must affect the sustenaibility of the turbulence. We turn to higher resolution simulations to assess if our results can improve.

4.4. *High resolution MFM runs*

In order to maintain good resolution over the course of the simulations, thus avoiding expansion resulting from heat transport triggered by turbulence, we add an *ad hoc* cooling term as in Noble et al. (2010); Parkin & Bicknell (2013),

$$\frac{du_{cool}}{dt} = -\frac{u - u_{init}}{\tau_{cool}} \tag{20}$$

where $\tau_{cool} = 2\pi/\Omega$, and u_{init} is the initial specific internal energy constant. This fast cooling maintains the disk scale height nearly constant, thus preserving the initial resolution across the disk. In addition we increase the number of elements to 3 million which results in $\langle Q_y \rangle \sim 30, \langle Q_z \rangle \sim 10$ in the turbulent state.

In figure 11 various flow properties are plotted. The most important result is that the MRI turbulence is sustained for a longer time (as it should if the method is converging properly). During this phase the main flow diagnostics are in good agreement with those of grid code runs: $\alpha_M \sim 0.4$, the averaged magnetic energy is a few percent of the gas pressure, and the Maxwell stress about 4 times larger than the Reynolds stress (Hawley et al. 2011). In figure 11, the butterfly diagram is reproduced but after $300\Omega^{-1}$ the pattern becomes erratic. Comparing to the 1.5M elements MFM fiducial model in figure 9, finer magnetic field structures are captured (see figure 12) and the butterfly diagram/dynamo is better resolved. We note that even this simple cooling can introduce additional numerical noise at the kernel scale (Rice et al. 2014). However, we cannot afford higher resolution, or to run longer simulations, with this set-up (see section 5.1).

5. DISCUSSION

5.1. *Computational Cost and Possible Applications*

In addition to robustness of numerical results, another worthy metric of comparison between codes is their computational cost to carry out a comparable calculation. Here one should remember that particle-based codes such as MFM employ adaptive timesteps while eulerian codes, unless they use AMR or nested grids, do not. Adaptive timesteps allow particle-based codes, as well as AMR eulerian codes, to model successfully highly inhomogeneous flows with high dynamic range, therefore to some extent comparisom of computational efficiency in a relatively uniform fow condition as in the shearing boxes of this work does not do justice to the capabilities of spatially and temporally adaptive codes to which MFM belongs to.

In any case, we run a setup equivalent to our 3M elements local stratified simulation with ATHENA, and compare the computational cost directly using a fixed timestep in both. We found that the MFM simulation is $>$ 100 times more computationally expensive than an equivalent run with 32 cells per scale height using ATHENA with the orbital advection method (Masset 2000; Stone & Gardiner 2010) for optimization. The lower computationally efficiency of MFM has nothing to do with the hydro solver, rather owes to the neighbor "search tree" which needs to be updated constantly and walked to find neighbors and re-build the domain (because it allows for arbitrary particle re-configuration between timesteps). Of course, in simulations where particle order is not dramatically changing, and the only forces are local, we could in principle save considerable computational expense by simply storing the interacting neighbor lists and re-building the domain less often. Furthermore, there is room to improve significantly the neighbor search algorithm on modern massively parallel architectures coupled with accelerators, as it is being currently investigated for a range of particle-based codes (Guerrera et al. 2018).

Nevertheless, such a difference in performance is highly problem-dependent. The tree algorithm can be efficiently exploited – and the difference in performance is dramatically mitigated – if other physics which involves non-local forces is calculated. A prime example of the latter is self-gravity. The tree-based gravity solver coupled with MFM, indeed, is, generally speaking, both faster and more accurate compared

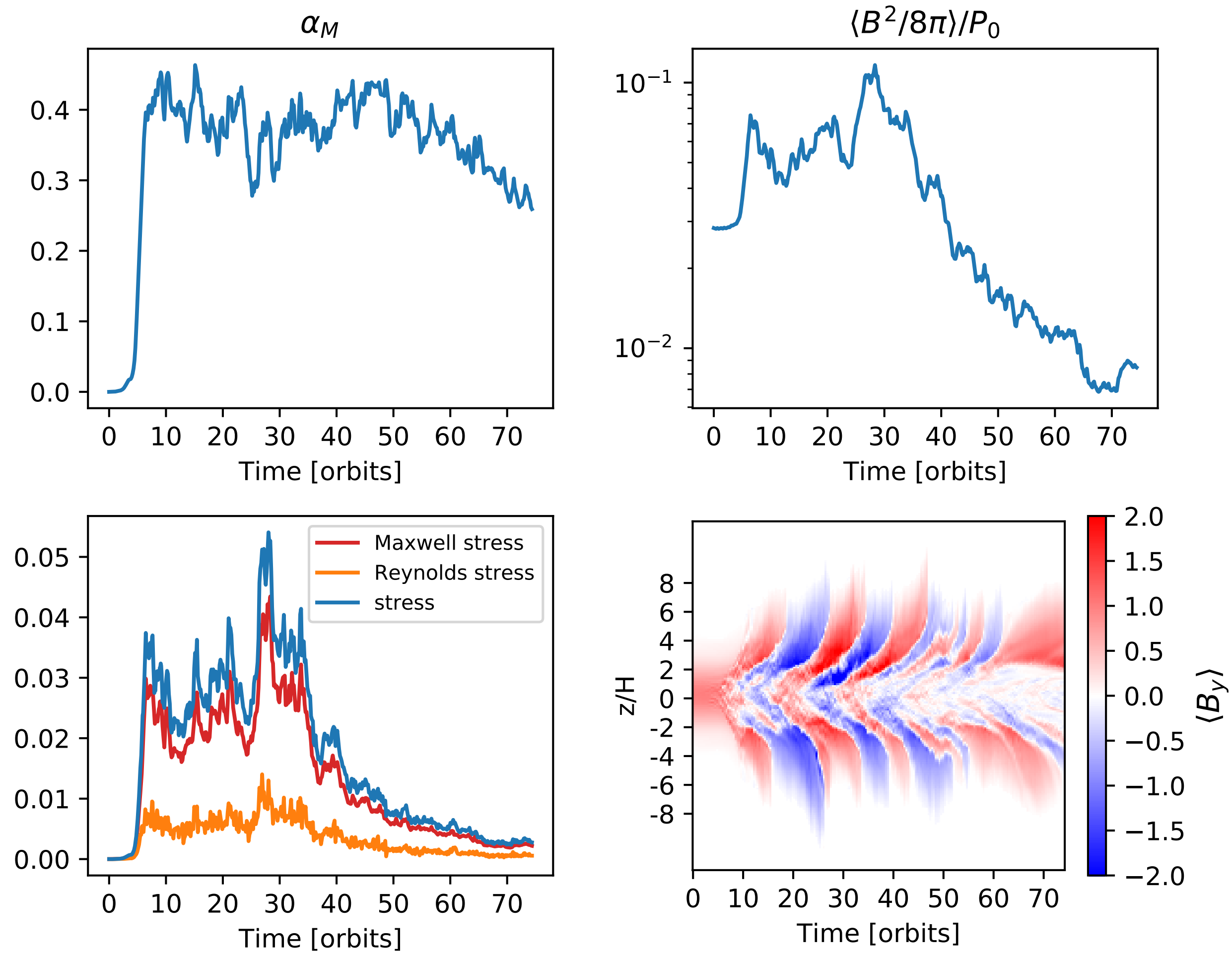

Figure 11. The evolution of magnetic fields in the high resolution (3M elements) MFM stratified shearing box simulation. The saturated α_M is ∼0.4 with $\langle\beta\rangle \sim 100$. The Maxwell stress is roughly four times of the Reynolds stress as found in Hawley et al. (1996). All stresses are normalized by P_0. The butterfly diagram becomes irregular at ∼50 orbits.

to traditional gravity solvers coupled with grid-based codes, which is the reason why particle-based methods with tree-based gravity have been since long very competitive in comparison with grid-based methods in the modeling of self-gravitating protoplanetary disks (see e.g. Mayer & Gawryszczak 2008). Furthermore, addressing self-gravitating disks ultimately requires global calculations (Durisen et al. 2007). This is by itself a natural regime for mesh-free codes since one of their major goals is to enable adaptive resolution on global problems, more akin to adaptive-mesh-refinement codes, which have similar computational and memory cost.

The most interesting applications of the mesh-free methods studied here are thus not in idealized MRI setups where accuracy of the MHD calculation over long timescales, absent other physical effects, is the prime objective. Rather, these methods may be more promising for studies of turbulence in magnetized self-gravitating disks, especially the strong dynamo action reported by Riols & Latter (2018). This spiral wave dynamo is vigorous even with large magnetic resistivity and may be responsible for the primordial magnetic field amplification in galaxy formation (Rieder & Teyssier 2016, 2017), a field where adaptive resolution (either with Lagrangian or AMR-type codes) is essentially required. Likewise, the methods described in this paper have considerable potential for applications in other areas of astrophysics where self-gravitating magnetized disks should be relevant, such as the central regions of massive protogalaxies where self-gravitating circumnuclear gas disks could trigger the formation of supermassive black holes (Regan & Haehnelt 2009; Choi et al. 2013; Mayer et al. 2010,

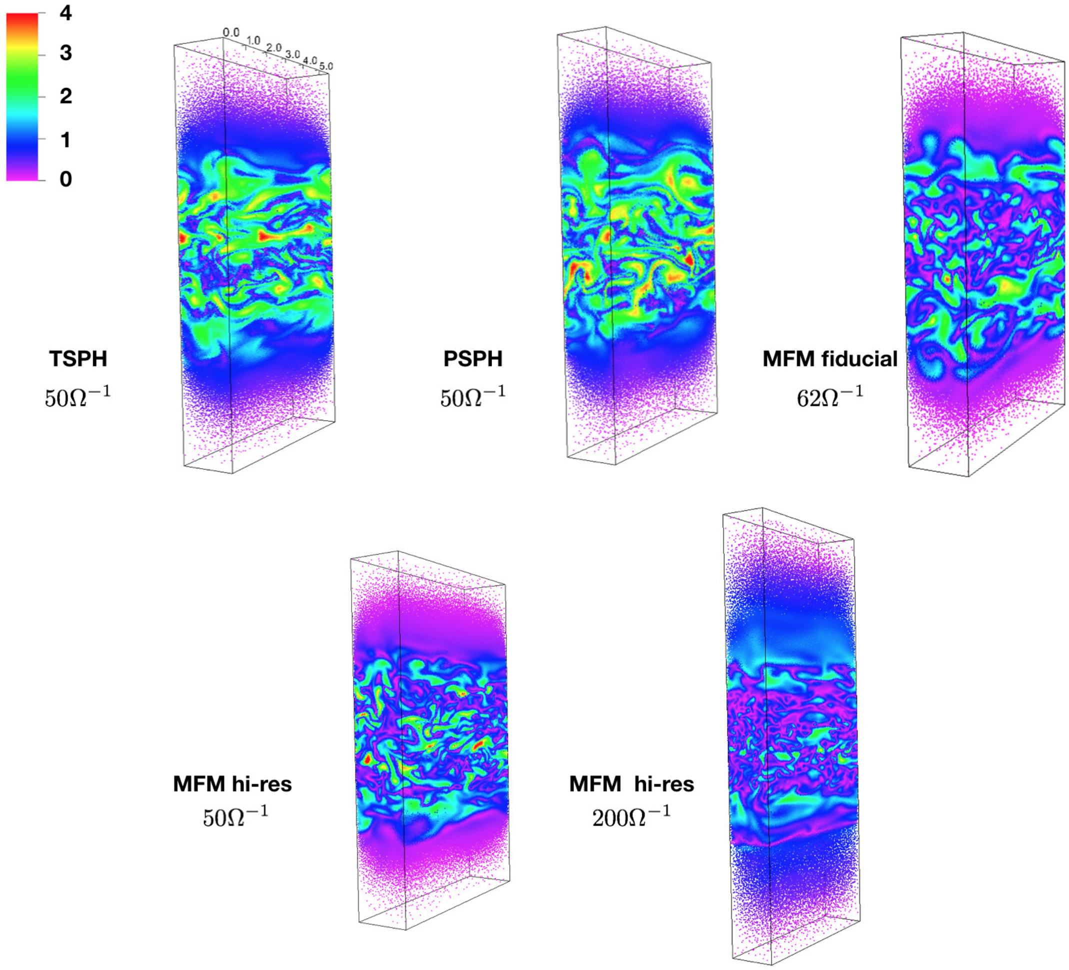

Figure 12. Fully developed MRI turbulence. Snapshots of magnetic field strength for a few stratified runs in table 1 as labeled beside the panels (note the field strength is shown in Gauss and $\beta = 1$ corresponds to magnetic field strength of 5 Gauss here). The upper panels are the fiducial 1.5M elements MFM simulation and its equivalent SPH simulations. The MFM snapshot is taken later than the SPH snapshots because the instability develops early in SPH due to stronger numeric noise (see figure 7, 9). The snapshots are taken roughly when α_M reaches its maximum. Comparing to SPH simulations, MFM captures finer magnetic field structures and shows less noise in the fields. In the lower panels, the higher resolution stratified shearing box (3M elements) captures even finer structures.

2015) or the outer regions of accretion disks around AGNs (Rafikov 2001). In the case of the protogalactic nuclei, in particular, adaptivity is necessary to capture a wide range of spatial and temporal scales. Furthermore, understanding the interplay between the stabilizing effect of magnetic pressure, turbulence and gas inflows governed by global self-gravitating modes might be the key to understand whether a monolithic central collapse into a supermassive star occurs, which later will turn into a massive black hole, as opposed to fragmentation into stars (Latif et al. 2014). The Riols & Latter dynamo action might play an important role in this latter case as it might reveal itself as an important element to understand the process of angular momentum transport, and thus the evaluate better the possibility of a central monolithic collapse.

5.2. *Other Lagrangian MHD methods*

We have restricted our study to just two classes of numerical methods, SPH and MFM (although we did consider a few “variants” of SPH). Furthermore, we only considered TSPH and PSPH variants of the SPH method. We should point out that caution is warranted in generalizing any of these results to other Lagrangian methods. Moving meshes or mesh-free finite-volume (MFV)-type methods with divergence-cleaning methods can arbitrarily “smooth” the mesh motion, decreasing the “mesh deformation noise” (McNally et al. 2012; Muoz et al. 2014) and likely allowing for more accurate divergence cleaning simply because the mesh is deforming less rapidly and less irregularly (so e.g. smaller gradient errors can be ensured). As noted above, unstaggered CT schemes have now been developed (Mocz et al. 2014, 2016) for certain specific types of moving-mesh schemes, which can maintain $\nabla \cdot \mathbf{B} \approx 0$ at machine precision, so should perform more similarly to CT-grid schemes here, although the numerical noise/dissipation properties of moving-mesh codes (which determine the MRI damping) are often very different.

Fundamentally distinct SPH MHD methods have also been developed. Although early attempts at implementing SPH MHD based on vector potentials did not allow reconnection (e.g. Rosswog & Price 2007), newer hybrid methods that combine vector potentials with divergence-cleaning in the vector potential space appear to avoid exactly the runaway field amplification discussed here (see Stasyszyn & Elstner 2015). To our knowledge, however, these schemes have not yet been explored in a broader context or used for MRI simulations. Finally, in the final stages of the preparation of this paper we became aware that a simple variant of an SPH MHD solver based on the GDSPH method in the GASOLINE2 code (Wadsley et al. 2017) is currently being tested in local MRI setups similar to those described here (Robert Wissing et al, private communication). In the latter, the Lorentz force is smoothed in the same way as the hydro force, possibly helping to reduce numerical dissipation.

6. CONCLUSIONS

We presented the results of a series of MRI simulations with two meshless MHD methods, SPH and MFM, in both vertically unstratified and stratified boxes. Two variants of SPH were considered, a “vanilla” SPH method based on the density-energy formulation, and PSPH (both as implemented in the GIZMO code). The MRI, especially in its zero-net-flux configuration, is sensitive to numerical or physical dissipation which makes it challenging for mesh-free codes to adequately simulate it, because of their relatively high level of numerical noise.

Our main findings can be summarized as:

1. The use of an appropriate kernel function which does not exhibit the pairing instability and allows a relatively large radius of compact support (e.g. Wendland C4) is crucial for maintaining element or mesh-generating-point order and for accurate gradient calculation. In MFM, this is directly akin to using a larger stencil to obtain more accurate, higher-order gradient estimators in traditional regular-grid codes. Although these kernels are less compact than the traditional spline kernels and tend to over-smooth fluid variables in SPH, they help to sustain the turbulence longer.

2. A stiff adiabatic EOS can help to control the noise in solving the energy equation where the truncation errors can be significant, because the magnetic energy is much smaller than the internal energy.

3. In unstratified shearing boxes with a net vertical field, MFM exhibits a similar error scaling in the linear growth MRI rates compared to the finite volume Eulerian code ATHENA. Both SPH and MFM can adequately simulate the ensuing turbulence, though the former is more diffusive and thus the MRI is closer to criticality. Two consequences of higher diffusivity in SPH are more vigorous channel bursts and very severe heating.

4. In unstratified shearing boxes with zero-net vertical field, SPH and MFM exhibit decaying turbulence at the (relatively low) resolution we are able to simulate here. It is possible this decay is linked to a very low numerical magnetic Prandtl number, but it is more likely that the numerical resistivity in MFM is simply too high at this resolution for sustaining the MRI.

5. In vertically stratified shearing box simulations, SPH MHD produces radically unphysical behaviour: turbulence dies out but strong toroidal fields continue to grow to equipartition with the gas pressure. This owes to non-trivial coupling of poorly-controlled magnetic field divergence, differential rotation/shear, and vertical stratification, at least in the most common SPH form of the induction and divergence-cleaning operators.

6. In vertically stratified shearing boxes, high resolution MFM simulations produce results comparable to grid codes implementing the CT cleaning method. For several tens of orbits the classical MRI dynamo is captured, with its characteristic butterfly diagram. Nonetheless, the turbulence ultimately dies out after some 50 orbits, at the relatively low resolution studied as our “baseline” here. Going to higher resolution sustains the dynamo for longer, indicating that the decay is likely due to residual numerical resistivity.

We thank Matthew Bate, Daniel Price, Stephen Rosswog, Jim Stone, James Wadsley, Sijing Shen and Robert Wissing for useful discussions. We acknowledge support from the Swiss National Science Foundation via the NCCR PlanetS. Support for PFH was provided by an Alfred P. Sloan Research Fellowship, NSF Collaborative Research Grant #1715847 and CAREER grant #1455342, and NASA grants NNX15AT06G, JPL 1589742, 17-ATP17-0214.

Software: GIZMO code (Hopkins 2015), VisIt

REFERENCES

Armitage, P. J. 1998, The Astrophysical Journal Letters, 501, L189

Bai, X.-N. 2014, The Astrophysical Journal, 791, 137

Bai, X.-N., & Stone, J. M. 2011, The Astrophysical Journal, 736, 144

—. 2013, The Astrophysical Journal, 767, 30

Bauer, A., & Springel, V. 2012, Monthly Notices of the Royal Astronomical Society, 423, 2558

Bodo, G., Cattaneo, F., Mignone, A., & Rossi, P. 2014, The Astrophysical Journal Letters, 787, L13

Bodo, G., Mignone, A., Cattaneo, F., Rossi, P., & Ferrari, A. 2008, Astronomy & Astrophysics, 487, 1

Brandenburg, A., & Dobler, W. 2002, Computer Physics Communications, 147, 471

Brandenburg, A., Nordlund, A., Stein, R. F., & Torkelsson, U. 1995, The Astrophysical Journal, 446, 741

Choi, J.-H., Shlosman, I., & Begelman, M. C. 2013, The Astrophysical Journal, 774, 149

Cullen, L., & Dehnen, W. 2010, Monthly Notices of the Royal Astronomical Society, 408, 669

Davis, S. W., Stone, J. M., & Pessah, M. E. 2010, Astrophys. J., 713, 52

Dedner, A., Kemm, F., Kröner, D., et al. 2002, Journal of Computational Physics, 175, 645

Dehnen, W., & Aly, H. 2012, Mon. Not. R. Astron. Soc., 425, 1068

Deng, H., Mayer, L., & Meru, F. 2017a, The Astrophysical Journal, 847, 43

Deng, H., Reinhardt, C., Benitez, F., Mayer, L., & Stadel, J. 2017b, arXiv preprint arXiv:1711.04589

Dobbs, C., Price, D., Pettitt, A., Bate, M. R., & Tricco, T. 2016, Monthly Notices of the Royal Astronomical Society, 461, 4482

Dolag, K., & Stasyszyn, F. 2009, Monthly Notices of the Royal Astronomical Society, 398, 1678

Durisen, R. H., Boss, A. P., Mayer, L., et al. 2007, Protostars and Planets V, 607

Evans, C. R., & Hawley, J. F. 1988, Astrophys. J., 332, 659

Fleming, T. P., Stone, J. M., & Hawley, J. F. 2000, The Astrophysical Journal, 530, 464

Forgan, D., Price, D. J., & Bonnell, I. 2016, Monthly Notices of the Royal Astronomical Society, 466, 3406

Fromang, S., Latter, H., Lesur, G., & Ogilvie, G. I. 2013, Astronomy & Astrophysics, 552, A71

Fromang, S., & Nelson, R. P. 2006, Astronomy & Astrophysics, 457, 343

Fromang, S., & Papaloizou, J. 2007, Astron. Astrophys., 476, 1113

Fromang, S., Papaloizou, J., Lesur, G., & Heinemann, T. 2007, Astron. Astrophys., 1132, 1123

Gaburov, E., & Nitadori, K. 2011, Mon. Not. R. Astron. Soc., 414, 129

Goldreich, P., & Lynden-Bell, D. 1965, Monthly Notices of the Royal Astronomical Society, 130, 125

Goodman, J., & Xu, G. 1994, The Astrophysical Journal, 432, 213

Gressel, O. 2013, The Astrophysical Journal, 770, 100

Guerrera, D., Maffia, A., & Burkhart, H. 2018, Data in brief, 20, 1148

Hawley, J. F. 2000, Astrophys. J., 528, 462

Hawley, J. F., Gammie, C. F., & Balbus, S. a. 1995, Astrophys. J., 440, 742

—. 1996, Astrophys. J., 464, 690

Hawley, J. F., Guan, X., & Krolik, J. H. 2011, Astrophys. J., 738, doi:10.1088/0004-637X/738/1/84

Hietel, D., Steiner, K., & Struckmeier, J. 2000, Mathematical Models and Methods in Applied Sciences, 10, 1363

Hopkins, P. F. 2012, Monthly Notices of the Royal Astronomical Society, 428, 2840

—. 2015, Monthly Notices of the Royal Astronomical Society, 450, 53

—. 2016a, Monthly Notices of the Royal Astronomical Society, 462, 576

—. 2016b, Monthly Notices of the Royal Astronomical Society, 466, 3387

—. 2017, arXiv preprint arXiv:1712.01294

Hopkins, P. F., & Raives, M. J. 2015, Monthly Notices of the Royal Astronomical Society, 455, 51

Hubber, D. A., Rosotti, G. P., & Booth, R. A. 2017, Monthly Notices of the Royal Astronomical Society, 473, 1603

Inutsuka, S.-I. 2002, Journal of Computational Physics, 179, 238

Lanson, N., & Vila, J.-P. 2008a, SIAM Journal on Numerical Analysis, 46, 1912

—. 2008b, SIAM Journal on Numerical Analysis, 46, 1935

Latif, M., Bovino, S., Van Borm, C., et al. 2014, Monthly Notices of the Royal Astronomical Society, 443, 1979

Latter, H. N., Lesaffre, P., & Balbus, S. A. 2009, Mon. Not. R. Astron. Soc., 394, 715

Latter, H. N., & Papaloizou, J. 2017, Monthly Notices of the Royal Astronomical Society, 472, 1432. http://dx.doi.org/10.1093/mnras/stx2038

Lesaffre, P., Balbus, S. A., & Latter, H. 2009, Monthly Notices of the Royal Astronomical Society, 396, 779

Lesur, G., Ferreira, J., & Ogilvie, G. I. 2013, Astronomy & Astrophysics, 550, A61
Lesur, G., Kunz, M. W., & Fromang, S. 2014, Astronomy & Astrophysics, 566, A56
Lesur, G., & Longaretti, P. Y. 2007, Mon. Not. R. Astron. Soc., 378, 1471
Lesur, G., & Ogilvie, G. 2008, Astronomy & Astrophysics, 488, 451
Masset, F. 2000, A&AS, 141, 165
Mayer, L., Fiacconi, D., Bonoli, S., et al. 2015, The Astrophysical Journal, 810, 51
Mayer, L., & Gawryszczak, A. J. 2008, in Astronomical Society of the Pacific Conference Series, Vol. 398, Extreme Solar Systems, ed. D. Fischer, F. A. Rasio, S. E. Thorsett, & A. Wolszczan, 243
Mayer, L., Kazantzidis, S., Escala, A., & Callegari, S. 2010, Nature, 466, 1082
McNally, C. P., Lyra, W., & Passy, J.-C. 2012, The Astrophysical Journal Supplement Series, 201, 18
Meheut, H., Fromang, S., Lesur, G., Joos, M., & Longaretti, P.-Y. 2015, Astronomy & Astrophysics, 579, A117
Miller, K. A., & Stone, J. M. 2000, Astrophys. J., 534, 398
Mocz, P., Pakmor, R., Springel, V., et al. 2016, Monthly Notices of the Royal Astronomical Society, 463, 477. http://dx.doi.org/10.1093/mnras/stw2004
Mocz, P., Vogelsberger, M., & Hernquist, L. 2014, Mon. Not. R. Astron. Soc., 442, 43
Muoz, D. J., Kratter, K., Springel, V., & Hernquist, L. 2014, Monthly Notices of the Royal Astronomical Society, 445, 3475. http://dx.doi.org/10.1093/mnras/stu1918
Noble, S. C., Krolik, J. H., & Hawley, J. F. 2010, The Astrophysical Journal, 711, 959
Pakmor, R., & Springel, V. 2013, Monthly Notices of the Royal Astronomical Society, 432, 176
Parkin, E., & Bicknell, G. 2013, The Astrophysical Journal, 763, 99
Pessah, M. E., & Goodman, J. 2009, The Astrophysical Journal Letters, 698, L72
Powell, K. G., Roe, P. L., Linde, T. J., Gombosi, T. I., & De Zeeuw, D. L. 1999, Journal of Computational Physics, 154, 284
Price, D. J. 2012, J. Comput. Phys., 231, 759
Price, D. J., & Bate, M. R. 2007, Mon. Not. R. Astron. Soc., 377, 77
—. 2008, Mon. Not. R. Astron. Soc., 385, 1820
—. 2009, Mon. Not. R. Astron. Soc., 398, 33
Rafikov, R. R. 2001, Monthly Notices of the Royal Astronomical Society, 323, 445. http://dx.doi.org/10.1046/j.1365-8711.2001.04201.x
Read, J., Hayfield, T., & Agertz, O. 2010, Monthly Notices of the Royal Astronomical Society, 405, 1513
Regan, J. A., & Haehnelt, M. G. 2009, Monthly Notices of the Royal Astronomical Society, 396, 343
Rice, W., Paardekooper, S.-J., Forgan, D., & Armitage, P. 2014, Monthly Notices of the Royal Astronomical Society, 438, 1593
Rieder, M., & Teyssier, R. 2016, Monthly Notices of the Royal Astronomical Society, 457, 1722
—. 2017, Monthly Notices of the Royal Astronomical Society, 471, 2674
Riols, A., & Latter, H. 2018, Monthly Notices of the Royal Astronomical Society, 474, 2212. http://dx.doi.org/10.1093/mnras/stx2455
Rosswog, S. 2015, Monthly Notices of the Royal Astronomical Society, 448, 3628. +http://dx.doi.org/10.1093/mnras/stv225
Rosswog, S., & Price, D. 2007, Monthly Notices of the Royal Astronomical Society, 379, 915
Ryan, B. R., Gammie, C. F., Fromang, S., & Kestener, P. 2017, The Astrophysical Journal, 840, 6
Saitoh, T. R., & Makino, J. 2013, The Astrophysical Journal, 768, 44
Sano, T., Inutsuka, S.-i., Turner, N. J., & Stone, J. M. 2004, The Astrophysical Journal, 605, 321
Shi, J.-M., Stone, J. M., & Huang, C. X. 2015, Monthly Notices of the Royal Astronomical Society, 456, 2273
Simon, J. B., & Hawley, J. F. 2009, The Astrophysical Journal, 707, 833. http://stacks.iop.org/0004-637X/707/i=1/a=833
Simon, J. B., Hawley, J. F., & Beckwith, K. 2011, Astrophys. J., 730, 94
Simon, J. B., Lesur, G., Kunz, M. W., & Armitage, P. J. 2015, Monthly Notices of the Royal Astronomical Society, 454, 1117
Springel, V. 2005, Monthly notices of the royal astronomical society, 364, 1105
—. 2010a, Annu. Rev. Astron. Astrophys., 48, 391
—. 2010b, Mon. Not. R. Astron. Soc., 401, 791
Stasyszyn, F. A., & Elstner, D. 2015, Journal of Computational Physics, 282, 148
Steinacker, A., & Papaloizou, J. C. 2002, The Astrophysical Journal, 571, 413
Stone, J. M., & Gardiner, T. A. 2010, The Astrophysical Journal Supplement Series, 189, 142
Stone, J. M., Gardiner, T. A., Teuben, P., Hawley, J. F., & Simon, J. B. 2008, The Astrophysical Journal Supplement Series, 178, 137
Stone, J. M., Hawley, J. F., Gammie, C. F., & Balbus, S. A. 1996, The Astrophysical Journal, 463, 656

Teyssier, R. 2002, Astronomy & Astrophysics, 385, 337
Tricco, T. S., & Price, D. J. 2012, Journal of Computational Physics, 231, 7214
—. 2013, Monthly Notices of the Royal Astronomical Society, 436, 2810
Turner, N., Sano, T., & Dziourkevitch, N. 2007, The Astrophysical Journal, 659, 729
Vila, J. 1999, Mathematical models and methods in applied sciences, 9, 161
Wadsley, J. W., Keller, B. W., & Quinn, T. R. 2017, Monthly Notices of the Royal Astronomical Society, 471, 2357
Zhu, C., Pakmor, R., van Kerkwijk, M. H., & Chang, P. 2015, The Astrophysical Journal Letters, 806, L1
Zhu, Z., & Stone, J. M. 2018, The Astrophysical Journal, 857, 34

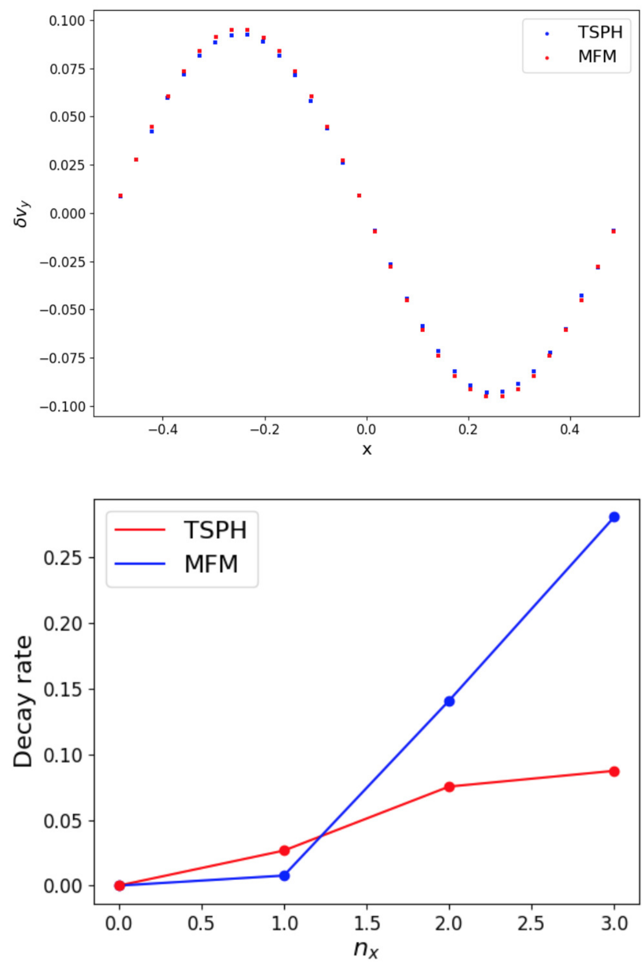

Figure 13. The velocity perturbation ($U = 0.1, n_x = 1$) decays slightly. In this test, the artificial viscosity is almost zero (in the Cullen & Dehnen switch $\alpha_{sph} = \alpha_{min} = 0.05$) and TSPH has a smaller numerical dissipation when the resolution is low.

APPENDIX

A. NUMERICAL VISCOSITY

To test the numerical viscosity we perturb the background shear flow by adding a radial dependent azimuthal velocity (a 'zonal flow'), ie, $\delta \boldsymbol{v} = U sin(2\pi n_x x)\hat{\boldsymbol{y}}$. We adjust the internal energy (for the EOS used here, $\gamma = 5/3$) so that the pressure perturbation is $\delta P = -\frac{\Omega U}{\pi n_x} cos(2\pi n_x x)$ and the initial setup is in equilibrium. Numerical viscosity will cause the perturbation to decay. By drawing an analogy to the Navier-Strokes equations (not necessarily true here), U will decay at a rate $\nu_{num} k_x^2$, where ν_{num} is the effective numerical viscosity and $k_x = 2\pi n_x$. We fit the decay of $\langle(\delta v_y)^2\rangle$ to determine ν_{num} and the decay rate of $\langle(\delta v_y)^2\rangle$ is shown in figure 13. We use a shearing box of size $H \times H \times H$ resolved by $32 \times 32 \times 32$ elements to carry out simulations with $U = 0.1$ and $n_x = [1, 2, 3]$. In figure 13, the numerical viscosity in MFM is larger than TSPH when the resolution is low. However, MFM outperforms TSPH at 32 elements per wavelength which is in line with the channel flow growth rate test in section 2.4.

B. NUMERICAL RESISTIVITY

Numerical dissipation can destroy magnetic fields. In a periodic box of size $H \times H \times H$ resolved by $32 \times 32 \times 32$ elements, we initial vertical magnetic fields and adjust the internal energy to set the box in pressure equilibrium. Here we set $\gamma = 5/3$ but tests with an isothermal EOS behave similarly. The fields take the form of $\boldsymbol{B} = B_0 \hat{\boldsymbol{z}} sin(2\pi n_x x)$, where $B_0 = \sqrt{8\pi P_0/\beta}$. In MFM simulations, the field structure decays due to numerical resistivity (see figure 14). B_0 should decay at a rate $\eta_{num} k_x^2$. The decay rate can be determined by fitting the decay of the averaged magnetic energy

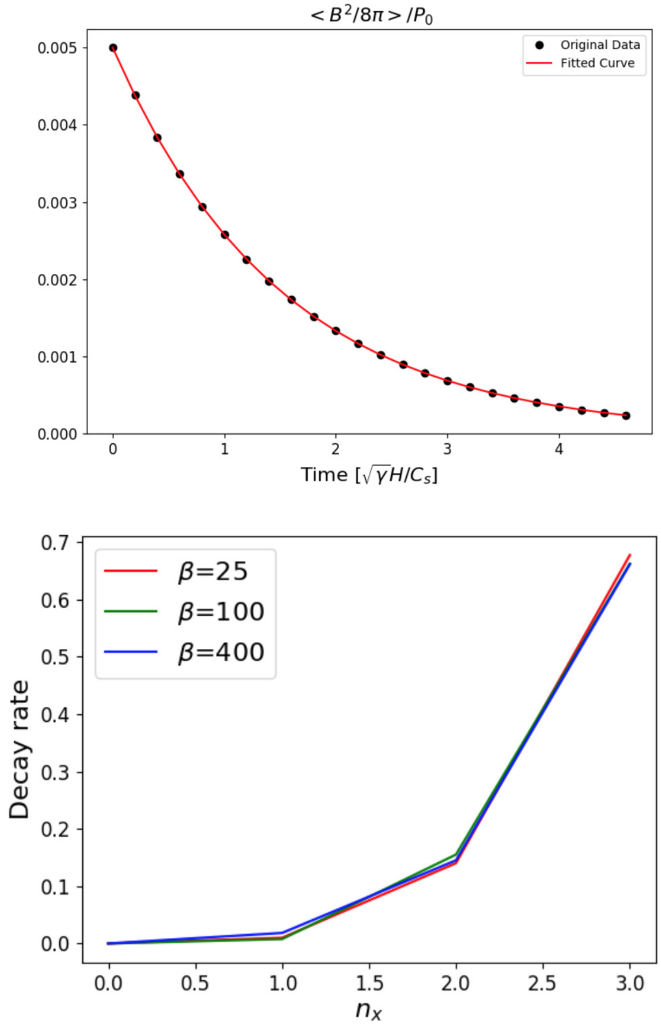

Figure 14. The magnetic energy decays exponentially in the test with $\beta = 100, n_x = 3$. We fit the curve to an exponential function to get the decay rate. The decay rate increase fast (fater than a parabola) as the resolution decreases, i.e., n_x increases; it is almost independent of the magnetic field strength in our tested range.

(decays twice as fast as B_0). We vary the wavelength (n_x) and field strength (β) to test how strong the numerical dissipation is. In this test, the dimensionless divergence of the magnetic fields is $\sim$0.0001 and we believe the dissipation is not caused by the non-zero divergence. However, in SPH simulations the magnetic energy doesn't decay even with $n_x = 3$ (see figure 15). The numerical noise from the artificial viscosity and resistivity break the perfect lattice.

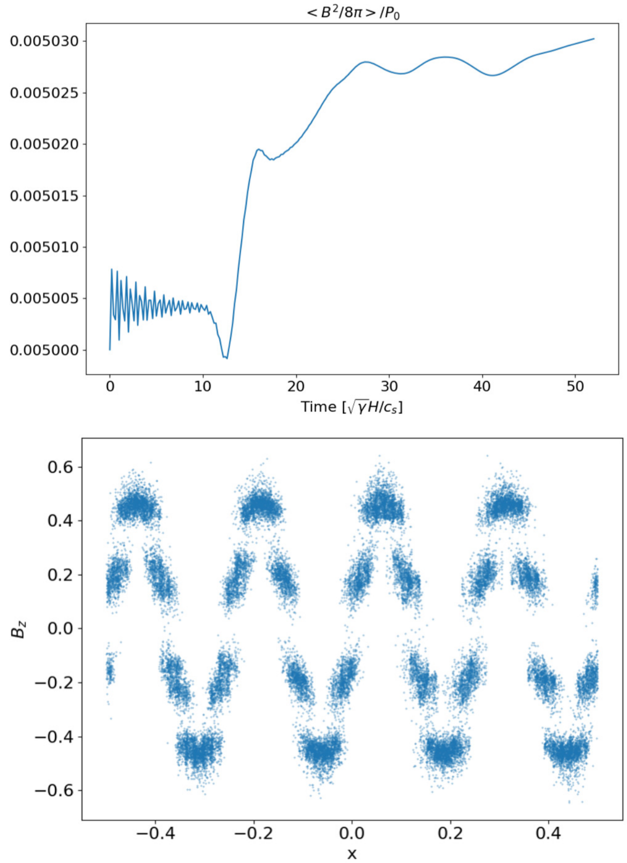

Figure 15. The magnetic energy doesn't decay in the TSPH test with $\beta = 100, n_x = 3$. But the magnetic field structure becomes noise at $50\sqrt{\gamma}H/c_s$